Assessment of teleseismically-determined source parameters for the April 25, 2015 M_W 7.9 Gorkha, Nepal earthquake and the May 12, 2015 M_W 7.2 aftershock

Thorne Lay [a,*], Lingling Ye [b], Keith D. Koper [c], Hiroo Kanamori [b]

[a] Department of Earth and Planetary Sciences, University of California Santa Cruz, Santa Cruz, CA 95064, USA
[b] Seismological Laboratory, California Institute of Technology, Pasadena, CA 91125, USA
[c] Department of Geology and Geophysics, University of Utah, Salt Lake City, UT 84112, USA

ARTICLE INFO

ABSTRACT

On April 25, 2015 a major (M_W 7.9) thrust earthquake ruptured the deeper portion of the seismogenic plate boundary beneath Nepal along which India is underthrusting Eurasia. An M_W 7.2 aftershock on May 12, 2015 extended the eastern, down-dip edge of the rupture. These destructive events caused about 9000 fatalities and 23,000 injuries. The overall rupture zone is about 170 km long and 40–80 km wide. This region of the plate boundary previously experienced a large earthquake in 1833, and in 1934 a larger M_S 8.0 event located to the east ruptured all the way to the surface. The Main Himalayan Thrust (MHT) on which slip occurred in 2015 has a very low dip angle of ~6°, and the depth of the mainshock slip distribution is very shallow, extending from ~7 to ~18 km. The shallow dip and depth present challenges for resolving faulting characteristics using teleseismic data. We analyze global teleseismic signals for the mainshock and aftershock to estimate source parameters, evaluating the stability of various procedures used for remotely characterizing kinematics of such shallow faulting. Back-projection and finite-fault slip inversion are used to assess the spatio-temporal rupture history and evidence for frequency-dependent radiation along dip. Slip zone width constraints from near-field geodetic observations are imposed on the preferred models to overcome some limitations of purely teleseismic methods. Radiated energy, stress drop and moment rate functions are determined for both events.

1. Introduction

The continental collision zone along Nepal in which Indian lithosphere underthrusts a thrust duplex sequence now attached to Eurasia at about 20 mm/yr (Ader et al., 2012) experienced a major earthquake on April 25, 2015 [hypocenter: 28.230°N, 84.731°E, 8.2 ± 2.9 km deep, 06:11:25.95 UTC, m_b 7.1, M_S 7.9 (United States Geological Survey – USGS National Earthquake Information Center – NEIC: http://earthquake.usgs.gov/earthquakes/)]. An ~170 km long aftershock zone (e.g., Adhikari et al., 2015; Bai et al., 2016; Hayes et al., 2015) extends unilaterally east-southeast from the hypocenter, which was located 80 km northwest of the center of Kathmandu (Fig. 1). This included m_b 6.1 and M_W 6.7 aftershocks within 34 min of the mainshock located at opposite ends of the mainshock slip zone and an M_W 6.7 event located near the eastern end on April 26 (Fig. 1). On May 12, 2015 a very large aftershock [hypocenter: 27.809°N, 86.066°E, 15 ± 1.7 km deep, 07:05:19.730 UTC, m_b 6.8, M_S 7.6 (USGS-NEIC)] struck near the eastern end of the mainshock rupture, followed by an M_W 6.1 event about 32 min later (Fig. 1). With rupture zones underlying the northern portion of Kathmandu and the frontal ranges of the Himalayas (Fig. 1), these large earthquakes caused about 9000 fatalities and 23,000 injuries, extensive damage to more than 770,000 brick and stone masonry structures, and widespread landsliding (e.g., Bilham, 2015; Goda et al., 2015; Moss et al., 2015). Fortunately, high frequency ground motions were relatively weak in Kathmandu (e.g., Avouac et al., 2015a; Bhattarai et al., 2015; Dixit et al., 2015; Galetzka et al., 2015; Grandin et al., 2015; Hayes et al., 2015; Martin et al., 2015), limiting damage for urban reinforced concrete structures (Goda et al., 2015; Martin et al., 2015; Yun et al., 2015).

The continental collision zone in Nepal is recognized to be a region with potential for great earthquakes based on the occurrence of prior large earthquakes in 1255, 1344, 1505, 1833, and 1934 (e.g., Bilham, 1995; Bilham et al., 2001; Sapkota et al., 2013; Mugnier et al., 2013; Bollinger et al., 2014; Hayes et al., 2015). The historic events account for only a fraction of the plate convergence (e.g., Bilham and Ambraseys, 1995), but the shortfall is not a result of aseismic sliding. Geodetic measurements establish that the Main Himalayan Thrust (MHT) is fully locked along most of the boundary (e.g., Ader et al., 2012; Bollinger et al., 2016; Stevens and Avouac, 2015), so establishing the slip distributions for the 2015 earthquakes was an immediate priority for assessing how much accumulated strain was released.

* Corresponding author.
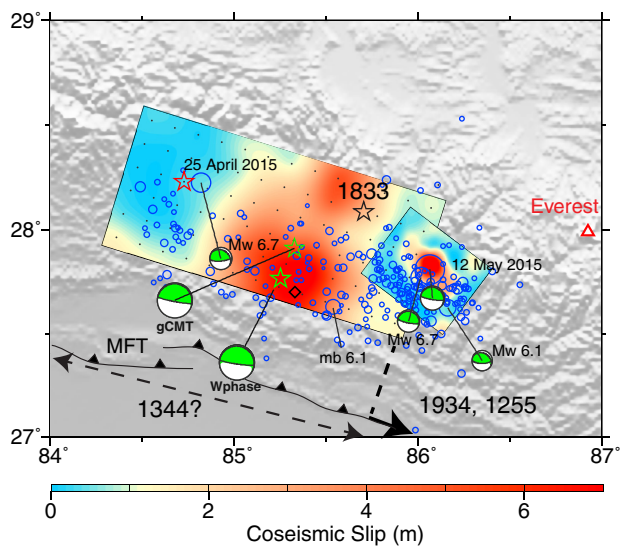 E-mail address: tlay@ucsc.edu (T. Lay).

Fig. 1. Map of the source region of the April 25, 2015 Gorkha, Nepal M$_W$ 7.9 earthquake, with the preferred teleseismic slip models for the mainshock and the May 12, 2015 M$_W$ 7.3 aftershock shown with color palettes. The red star is the epicenter for the mainshock from the USGS-NEIC. The black star is the approximate location of the 1833 epicenter. The dashed double-headed arrow indicates the approximate along-strike position of the 1344 earthquake. The black toothed curves indicate the outcrop of the Main Frontal Thrust (MFT). The solid black line with arrowhead indicates the region of surface ruptures of the 1934 and 1255 earthquakes ESE of the 2015 sequence. Blue circles indicate the USGS-NEIC locations of aftershocks in the first month after the event, scaled proportional to magnitude. Global centroid moment tensor (gCMT) solutions are shown in green for the mainshock and the four largest aftershocks, with the focal mechanisms plotted at the centroid locations or, for the mainshock, linked to a green star at the centroid location. The large aftershock locations from USGS-NEIC have tie-lines to the corresponding gCMT solutions. The mainshock W-phase solution is also shown and linked to the corresponding centroid location indicated by a green star. The red triangle indicates the location of Mount Everest. (For interpretation of the references to color in this figure legend, the reader is referred to the web version of this article.)

Many studies of global and regional seismic recordings, local high-rate GPS recordings, InSAR interferograms from Sentinel-1, RadarSat-2, and Advanced Land Observation Satellite-2 (ALOS-2) observations of surface offsets, and shaking intensity and damage patterns have been conducted, providing robust characterizations of the source processes and the overall earthquake sequence (e.g., Hough, 2015). The rupture did not reach to the surface (e.g., Angster et al., 2015), unlike the adjacent 1255 and 1934 (M$_S$ 8.0 ISC-GEM, Storchak et al., 2013) Bihar-Nepal ruptures (Fig. 1; Bollinger et al., 2014). The extensive quantification of the 2015 events provides an opportunity to evaluate source parameter estimates made just from teleseismic observations, both to quantify the far-field attributes of the sources for comparisons with other major earthquakes and to evaluate the limitations of teleseismic analyses that generally provide the most rapid source characterizations after a large damaging earthquake (many earthquakes do not have the robust geodetic information available for these Nepal events, and even those that do often lack rapid access to the data).

2. Long-period source parameters

Long-period seismic waves provide point-source characterizations of earthquakes, critical for event comparisons and providing reference parameters for ground motion assessments and fault model constraints. The primary solutions for the April 25, 2015 mainshock obtained by routine moment tensor inversion operations are listed in Table 1. All of the inversions yield almost pure double-couple thrust faulting solutions compatible with a planar rupture. The global Centroid-Moment Tensor (gCMT) solution and our W-phase inversion mechanisms are shown in Fig. 1 along with their centroid locations (green stars). Our W-phase inversion (Kanamori and Rivera, 2008; Duputel et al., 2012) used 134 global broadband stations with 213 separate components for the passband 1.67–10.0 mHz. The centroid time shifts in Table 1 are resolved within a few seconds uncertainty, making this a relatively robust source parameter (Duputel et al., 2013), while our analysis indicates that the centroid location parameters have at least ±0.3° epicentral uncertainty and ±5 km depth uncertainty, not accounting for reference model uncertainty. Hayes et al. (2015) and He et al. (2015) discuss the time evolution of the W-phase inversions for the mainshock, the most rapidly calculated faulting mechanisms, with the earliest solutions (within 20 min) being limited mainly by lack of availability of real-time access to nearby broadband seismic stations in India and China. Duputel et al. (2016) use spectral-element method computations for a 3-D Earth model to perform CMT inversion, finding that centroid depths between 8 and 14 km are preferred. Overall, the long-period seismic models indicate that the mainshock can generally be characterized as an M$_W$ 7.9 thrust event on a 5–7° dipping plane with centroid depth ≤ 25 km. Fault dip and seismic moment trade-off inversely for shallow dipping thrust events, which is important to consider if solutions using different dip values are compared with these results.

The long-period moment tensor inversions for the May 12, 2015 aftershock (Table 2) indicate that the event can be generally characterized as an M$_W$ 7.2 event on a 9–11° dipping plane with centroid depth ≤ 17.5 km. The gCMT solution is shown in Fig. 1. The strike is rotated ~15° clockwise and the rupture centroid is about 75 km east relative to the mainshock values. Given the lack of surface rupture, the along-dip extent of both ruptures is important to resolve.

3. Back-projection analyses for the mainshock

First introduced for the 2004 Sumatra earthquake rupture (Ishii et al., 2005; Krüger and Ohrnberger, 2005), various slant-stacking, array-processing, and compressive sensing procedures have been applied to track high-frequency radiation from large earthquakes with minimal a priori assumptions about the rupture kinematics. These approaches use either dense networks of stations for which the high-frequency signals are relatively coherent or global distributions of stations for which only the lower-frequency signals are relatively coherent to detect subtle move-out patterns of arrivals in the data. A horizontal grid of possible subevent locations across the source region is assumed and narrow band P wave energy is processed to isolate any discrete bursts of radiation in space and time. All such methods seek coherent

Table 1
Long-period point source moment tensor solutions for the April 25, 2015 mainshock.

Source	Moment (10^{20} Nm)	M$_W$	Best-double couple strike, dip, rake	Centroid location latitude, longitude, depth	Centroid time shift, s
gCMT[a]	8.39	7.88	287°, 6°, 96°	27.91°N, 85.33°E, 12 km	32.3
CNRS W-phase[b]	9.07	7.91	286.7°, 5.2°, 97.2°	27.77°N, 85.26°E, 25.5 km	32.2
NEIC W-phase[c]	6.62	7.81	290°, 7°, 101°	27.77°N, 85.18°E, 23.5 km	31.0
ERI W-phase[d]	8.83	7.90	290.3°, 5.1°, 100.4°	27.63°N, 85.10°E, 15.5 km	34.0
This study W-phase	9.63	7.92	287.0°, 7.0°, 98.7°	27.71°N, 85.22°E, 17.5 km	34.2

[a] http://www.globalcmt.org/CMTsearch.html
[b] http://wphase.unistra.fr/events/nepal_2015/index.html.
[c] http://earthquake.usgs.gov/earthquakes/.
[d] http://wwweic.eri.u-tokyo.ac.jp/WPHASE/global/20150425.0611/index.html

Table 2
Long-period point source moment tensor solutions for the May 12, 2015 aftershock.

Source	Moment (10^{19} Nm)	M_W	Best-double couple strike, dip, rake	Centroid location latitude, longitude, depth	Centroid time shift, s
gCMT[a]	8.84	7.23	307°, 11°, 117°	27.67°N, 86.08°E, 12 km	10.1
CNRS W-phase[b]	8.20	7.21	302.2°, 10.3°, 109.3°	27.44°N, 86.04°E, 17.5 km	9.0
NEIC W-phase[c]	9.89	7.26	303°, 9°, 110°	27.44°N, 85.96°E, 15.5 km	11.0
ERI W-phase[d]	9.60	7.25	298.9°, 7.6°, 95.6°	27.84°N, 85.82°E, 17.5 km	10.0

[a] http://www.globalcmt.org/CMTsearch.html
[b] http://wphase.unistra.fr/events/nepal_2015_aftershock/index.html.
[c] http://earthquake.usgs.gov/earthquakes/.
[d] http://wwweic.eri.u-tokyo.ac.jp/WPHASE/global/20150512.0705/index.html

high-frequency P wave arrivals in the signals, typically using ground velocity recordings, sometimes enhanced by non-linear n^{th}-root beam-forming. As a result, they detect localized rupture front accelerations and concentrated high slip velocity patches. Such imaging methods do not provide quantitative estimates of total slip and may fail to detect source radiation that is diffusely distributed over extended regions, but they do provide first-order information on the spatial extent of faulting and the apparent rupture expansion velocity for the sources of high-frequency radiation.

Numerous studies have presented imaging of the space–time pattern of coherent bursts of high-frequency P wave energy during the 2015 Nepal mainshock rupture. The Nepal source region is well situated with respect to concentrations of stations in Europe, Alaska/North America, China, Japan, and Australia; large aperture regional networks in each of these regions have been used for high-frequency imaging. There is also a fairly good azimuthal distribution of broadband stations available for global array imaging. Avouac et al. (2015a) used 0.5–2.0 Hz P wave energy for a station distribution in Australia and the Multiple Signal Classification (MUSIC) array processing method to image a narrow unilateral rupture ~150 km long expanding toward the ESE at 2.72 ± 0.13 km/s. Meng et al. (2015) used MUSIC for large aperture networks in Australia, North America and Europe, finding consistent
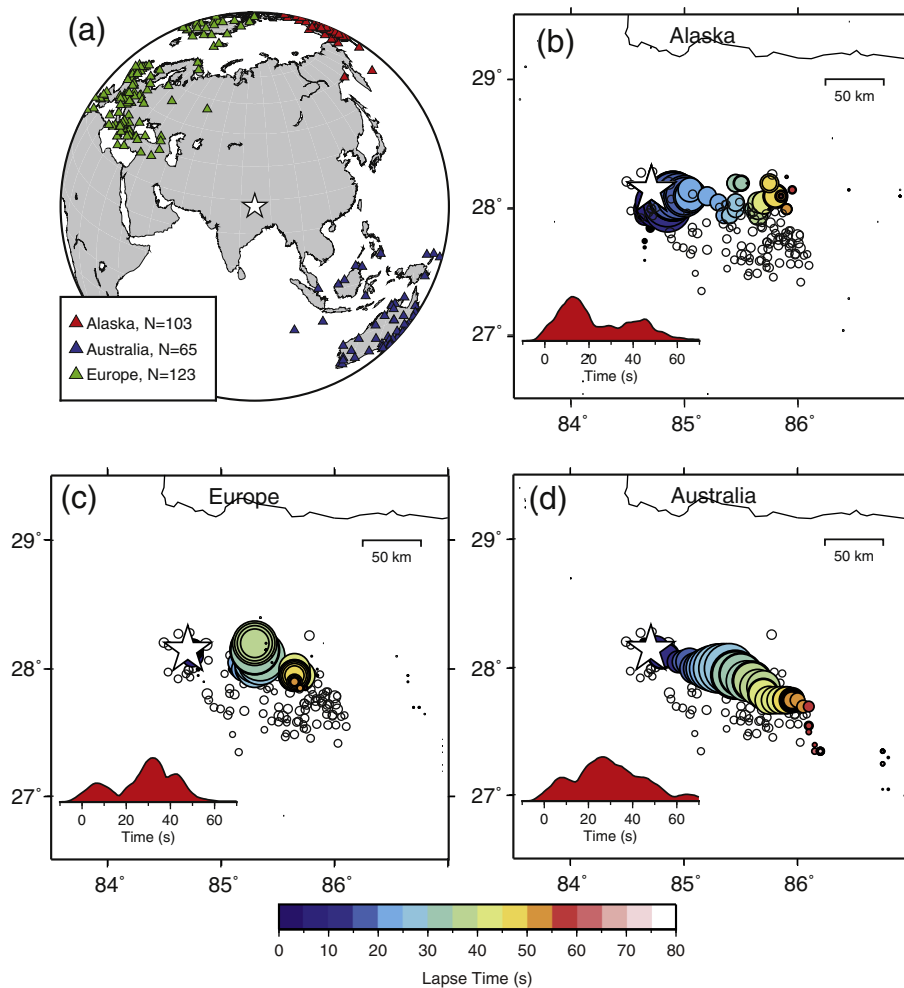

Fig. 2. Back-projection of teleseismic short-period P waves for the frequency band 1.0–3.0 Hz (Alaska) or 0.5–2.0 Hz (Europe and Australia) for three large networks with station locations (colored triangles, color-coded by network) shown in (a). The space–time sequences of short-period coherent energy pulses for networks in (b) Alaska, (c) Europe, and (d) Australia are shown with colored circles with varying lapse times and radii proportional to the fourth-root beam power in each 1 s time step. Aftershock locations prior to the 12 May 2015 aftershock are shown by the small black circles. The white stars indicate the mainshock epicenter. The red inset time series show the time evolution of relative maximum beam power in each back-projection image. (For interpretation of the references to color in this figure legend, the reader is referred to the web version of this article.)
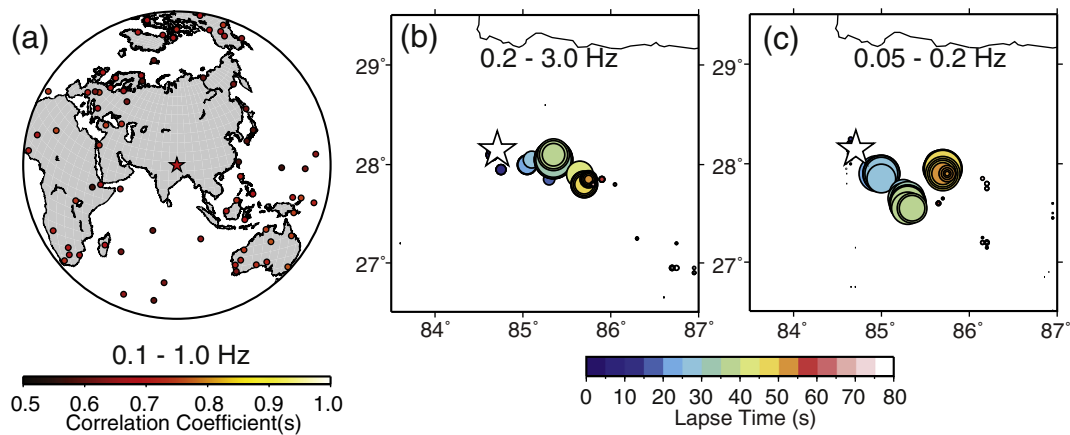
Fig. 3. Back-projection using a global distribution of broadband seismic stations (the same as used for P waves in the finite-fault inversions). (a) Map of the station locations (circles) relative to the mainshock epicenter (red star), color-coded by correlation coefficient relative to the average stack waveform. (b) Space–time sequence of peak back-projection beam power for the 0.2–3.0 Hz passband. The circles are color-coded for lapse time and scaled relative to peak beam power. (c) Space–time sequence of peak back-projection beam power for the 0.05–0.2 Hz passband. The circles are color-coded for lapse time and scaled relative to peak beam power. (For interpretation of the references to color in this figure legend, the reader is referred to the web version of this article.)

eastward rupture with variable inferred rupture speeds prior to applying relative network calibrations based on small aftershock images. The corrected patterns indicate a narrow unilateral rupture with a speed of 2.7 km/s. He et al. (2015) used similarly distributed networks obtaining space–time images that were deconvolved by individual network point-spread functions found by imaging a small aftershock. Analysis of the collective network images favor a 160 km long, narrow unilateral ESE rupture with a speed of 3.3 km/s. Wang and Mori (2016) used 0.2–2.0 Hz P waves from four networks comprised of stations in Australia, Europe, China and Japan, finding a lower rupture expansion of ~1 km/s in the first 20 s followed by expansion at 3 km/s for the next 30–40 s. Grandin et al. (2015) also show back-projections from several networks. Single- and multi-array compressive sensing methods, which invert for a parsimonious set of coherent subevents have yielded basically similar results (e.g., Yin et al., 2016; Liu and Ge, 2015), although rupture velocity estimates as low as 1.9 km/s have been obtained. Global array back-projection for the 0.2 to 3 Hz band by Fan and Shearer (2015) suggests unilateral eastward rupture expansion, whereas lower frequencies of 0.05 to 0.2 Hz were interpreted as a three-stage rupture with large subevents tens of kilometers to the south of the high-frequency subevents in the middle stage of the rupture, with variable interval rupture velocities of 2 to 4.6 km/s and an average value of about 2.9 km/s.

These results all show distinct subevents imaged from different networks. Efforts to improve the stability of the stacking algorithms by slowness filtering have been introduced (e.g., Meng et al., 2012). Application of a hybrid back-projection of global data for the mainshock that attempts to account for interference of depth phases by cross-correlating with Green's functions indicates a rupture velocity of 3 km/s (Yagi and Okuwaki, 2015). The latter study suggests that lower rupture velocities may result from misinterpreting coherent sP arrivals in terms of direct radiation from the rupture surface.

We demonstrate the behavior of high frequency back-projections for the April 25, 2015 mainshock using P-wave recordings from large aperture arrays in Alaska, Australia, and Europe (Fig. 2a). P-waves for stations at distances of 30°–95° from the epicenter are aligned within each regional array using multi-channel cross correlation (MCCC) of the first ten seconds of unfiltered, broadband traces (VanDecar and Crosson, 1990). Traces with low average correlation coefficients are removed and a desampling procedure is applied such that only the trace with the highest overall similarity with the average stack within an ~50 km scale geographical cell is retained.

For each regional array the P-energy is back-projected, using the approach of Xu et al. (2009), to a 2D grid of points in the source region that

are uniformly spaced at 0.05° in latitude and longitude. The aligned waveforms are band-pass filtered from 0.5 to 2.0 Hz for the Australia and Europe networks, and from 1 to 3 Hz for the Alaska network. Power is calculated from a tapered, 10-s long sliding window for a beam that is constructed with 4th-root stacking. Beams are reconstituted for each 1 s shift in origin time using source-receiver distances and MCCC-derived station corrections, so the back-projection times correspond to true origin times and not relative beam times. The beam peaks in each 1 s interval are plotted for each network in Fig. 2b,c,d, and animation of the images is provided in supplemental Animation S1. The images indicate a relatively simple rupture that progresses unilaterally to the ESE over a distance of ~150 km, in about 50–60 s, indicating a rupture velocity of ~3 km/s. The back-projection results from the three arrays are generally consistent and the source radiation zone correlates with the spatial extent of early aftershocks (black circles). However, the individual network estimates of signal coherence vary between arrays, as indicated by the peak beam power versus time plots and subevent radii in Fig. 2; this is a common finding and reflects the fact that each image involves a coherency measure influenced by azimuthally varying differences in depth phase interference, reference model inaccuracy, and blurring effects of the individual network responses.

We also used an array of broadband stations to form frequency-varying global back-projections. The station distribution is shown in Fig. 3a, and corresponds to the P wave data used in finite-fault inversions discussed below, which have careful relative alignments. We used a broader band 'high-frequency' passband of 0.2–3.0 Hz (Fig. 3b) given that the global distribution of stations causes incoherence of the higher frequencies, along with a 'low-frequency' passband of 0.05–0.2 Hz (Fig. 3c). Animations of the back-projections are shown in Animation S2. Time-varying beam peaks of the corresponding back-projections show significant differences, like those reported by Fan and Shearer (2015), with subevents imaged by lower frequencies shifting southward in the middle of the rupture. The very initial stage of radiation is weak for this earthquake, and we do not find clear evidence for early northward expansion of the rupture as suggested in 'Stage 1' of Fan and Shearer (2015); we consider that feature to be unresolved, and having very low seismic moment if it exists. The low-frequency passband is likely affected by coherent depth-phase interference due to the shallow dip. In general, we see relatively low frequency back-projection like this as problematic compared with more quantitative finite-fault inversion that explicitly accounts for variable Green's functions to different stations and across the fault model, but it does seem likely that there is a shift of low frequency radiation southward

in the central rupture zone. This is supported by analysis of directivity for a discrete low frequency arrival in the P waves noted by Wang and Mori (2016).

The differences in the high-frequency back-projections in Figs. 2 and 3 make it difficult to objectively combine the data to obtain a best over-all representation of the associated source process. Each network
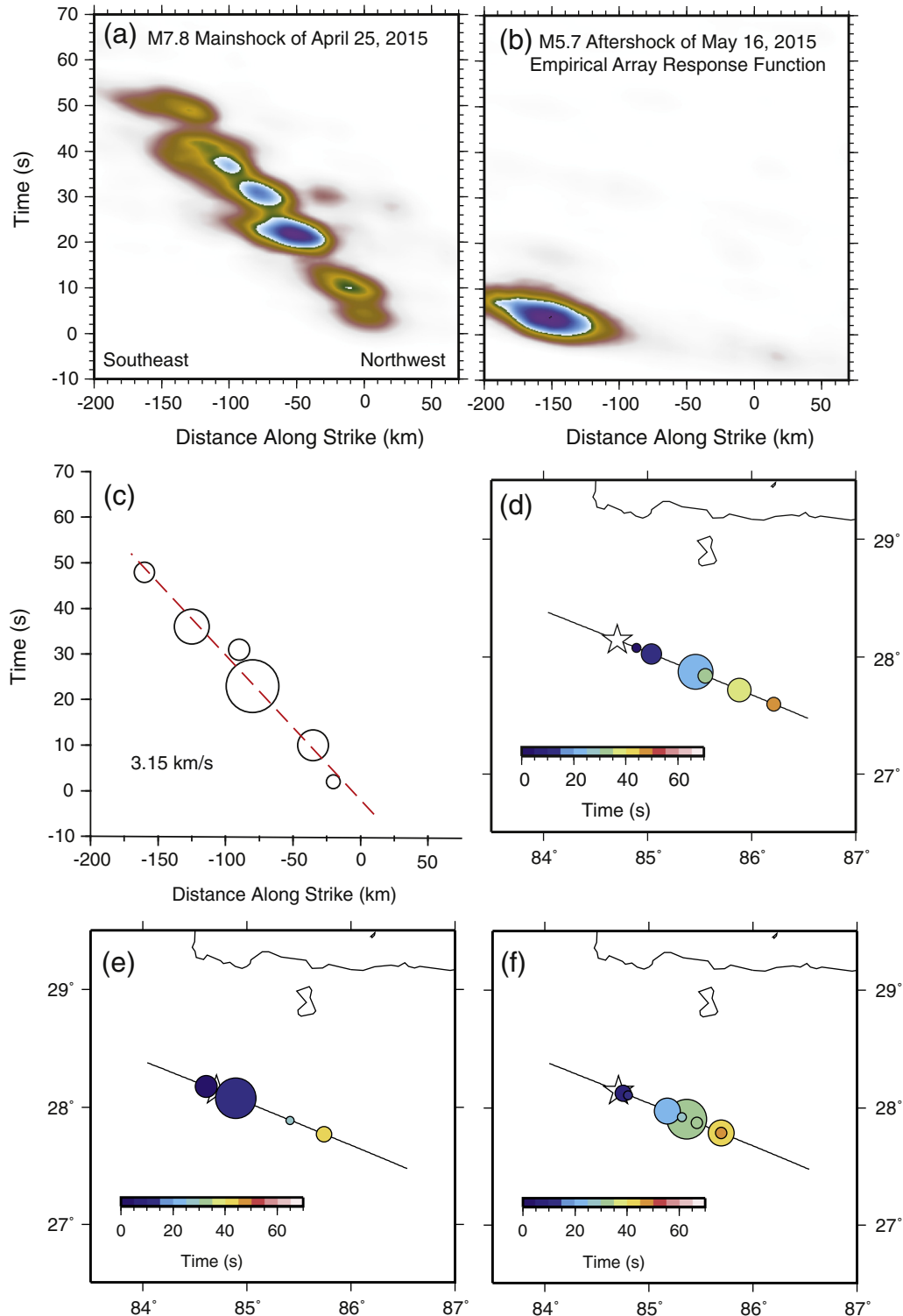

Fig. 4. Back-projection of 0.5–2.0 Hz P wave data recorded in the Australia region along a line of equally spaced points oriented in the strike direction (292°N), for the mainshock. (b) Similar linear back-projection for an M5.7 aftershock that occurred near the southeastern edge of the rupture area, which is used to calibrate the space–time point-spread function. (c) Subevent locations in space and time determined by deconvolving the aftershock image from the mainshock image. Circle size is proportional to relative beam power, and only subevents at least 20% as large as the maximum are retained. The dashed line shows a simple, unweighted least-squares fit to the subevent locations, giving the indicated effective rupture velocity. (d) Geographical presentation of subevents for the Australia data along the line of back-projection. Color indicates time and circle size is proportional to relative beam power. (e) Similar to (d) for the Alaskan network in Fig. 2. (f) Similar to (d) for the European network in Fig. 2. (For interpretation of the references to color in this figure legend, the reader is referred to the web version of this article.)
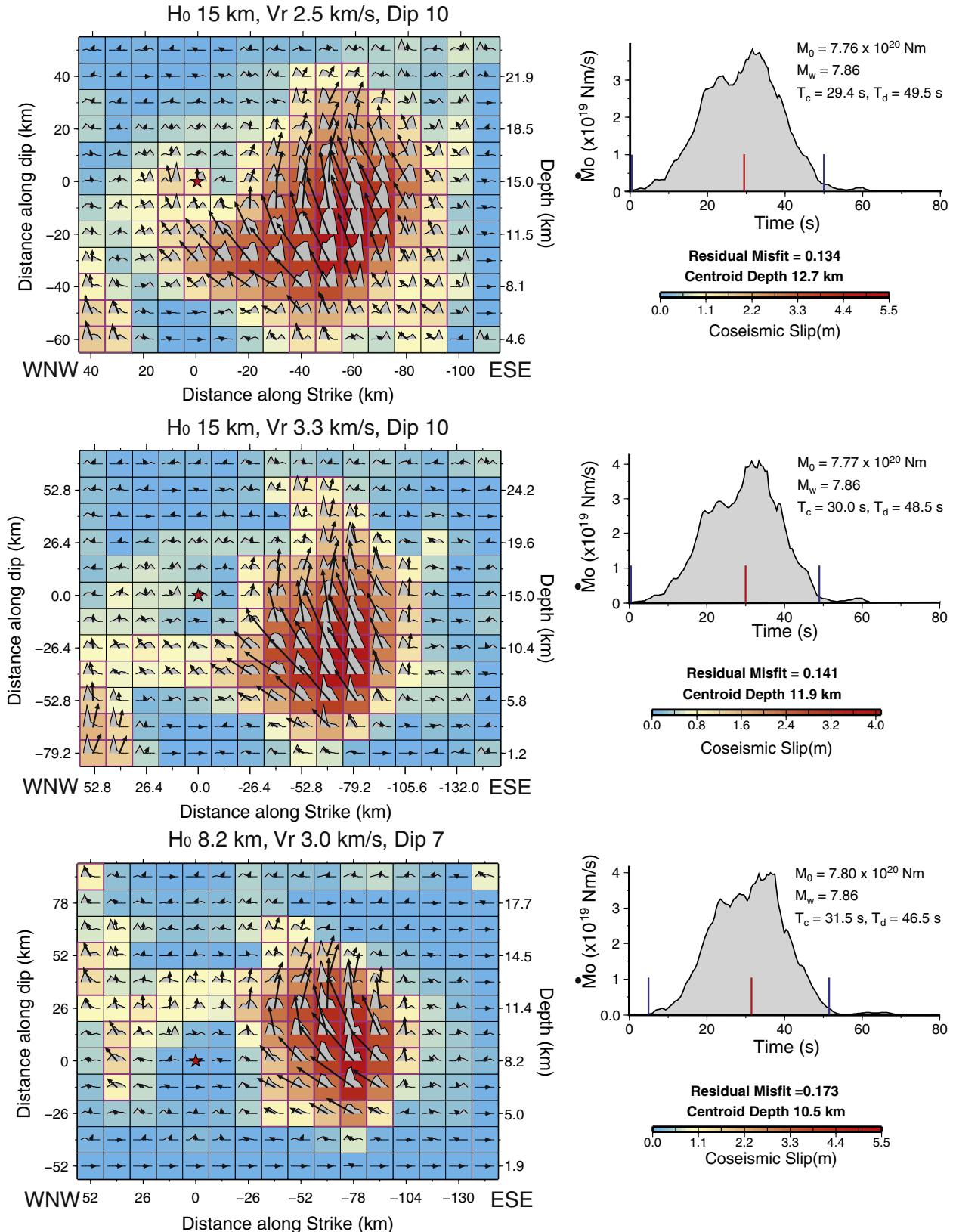
Fig. 5. Examples of slip models and corresponding moment-rate functions inverted from teleseismic P and SH waves for varying hypocentral depth, H_0, and rupture velocity, V_r, and fault plane dip. Subfault grids with colors and vector lengths indicating slip magnitude and variable subfault average rake direction (vector motion of the footwall (Indian plate) relative to the hanging wall (Eurasian plate)). The subfault moment rate functions are plotted within each cell, with maximum possible durations of 12.5 s. The red stars indicate the hypocenters. The grid spacing increases proportional to V_r. The red tick marks indicate the centroid time of the moment rate function, T_c, and the blue-ticks are hand-picked delimitations of the duration of the moment rate function, T_d. The residual waveform misfit for each inversion is shown along with the slip model centroid depth. (For interpretation of the references to color in this figure legend, the reader is referred to the web version of this article.)
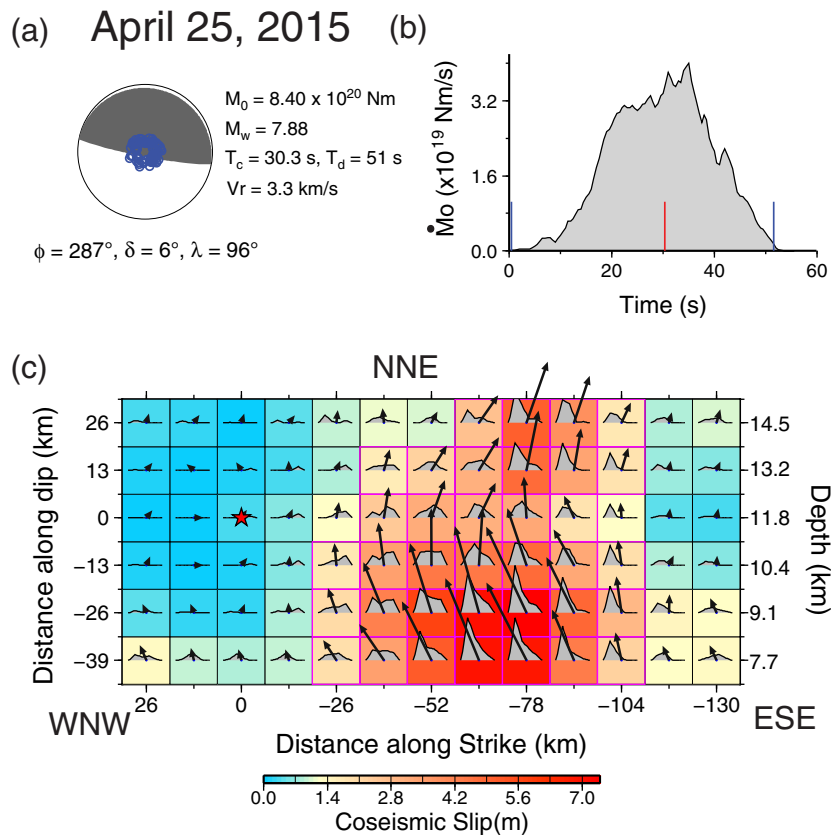
(a) April 25, 2015 (b)

$M_0 = 8.40 \times 10^{20}$ Nm
$M_W = 7.88$
$T_c = 30.3$ s, $T_d = 51$ s
$V_r = 3.3$ km/s

$\phi = 287°, \delta = 6°, \lambda = 96°$

Fig. 6. The finite-fault inversion of teleseismic P and SH waves for the April 25, 2015 event favored in this study. (a) The average focal mechanism of the rupture with the strike, $\phi = 287°$ and dip, $\delta = 6°$ indicates the planar fault geometry. The rake $\lambda = 96°$ is averaged from the variable rake inversion. (b) Moment-rate spectrum for the finite-fault model. The seismic moment was constrained from the gCMT inversion, corresponding to $M_W = 7.9$. The centroid time, T_c is indicated by red tick marks, and the total duration, T_d is bracketed by blue tick marks. (c) Subfault grid with colors and vector lengths indicating slip magnitude and variable subfault average rake direction (vector motion of the footwall (Indian plate) relative to the hanging wall (Eurasian plate)). The subfault moment rate functions are plotted within each cell, with maximum possible durations of 12.5 s. The red star is the hypocenter, at a depth of 11.8 km. The along-dip width of the model was constrained by the geodetic observations. This model is shown in map view in Fig. 1. The rupture front expansion velocity $V_r = 3.3$ km/s. (For interpretation of the references to color in this figure legend, the reader is referred to the web version of this article.)

samples different Green's functions and associated interference patterns, different slownesses due to distance range, and different network imaging artifacts that manifest in space–time blurring of coherence and misplaced projection of coherent depth-phase signal. To a large extent, these effects are relatively uniform for a given network for this predominantly unilateral, modest length rupture, with each subevent having similar image distortion at the network (Fig. 4a). To combine the various network images to obtain a more rigorous estimate of rupture velocity we estimate the individual network response by back-projection of corresponding bandwidth signals for an M_W 5.7 aftershock (Fig. 4b). We then deconvolve each effective array response, or point-spread function from the individual network images, extracting parsimonious models of the mainshock rupture (Fig. 4c). This deconvolution process helps to mitigate the smearing effects caused by depth phases and other near-source scattered energy in the P-coda. For simplicity, here we assume a common linear rupture dimension for all cases, validated by the degree to which each network's data form a linear trend in space–time (Fig. 4c) from which a rupture velocity can be estimated. This assumption suppresses relative slowness errors for different network configurations as it imposes relative consistency, but also likely gives an upper bound on the rupture velocity estimate. The resulting deconvolved images for the three arrays (Fig. 4d,e,f) and simultaneous least-squares regression of the discrete sub-events observed at the three arrays (He et al., 2015) gives a strike-averaged rupture velocity of 3.3 km/s along the ESE linear distribution. Even with the removal of the point-spread functions, the space–time subevent character differs between the networks, suggesting that one cannot reliably infer robust

discrete spatial attributes or variable rupture velocity of the high-frequency source process, but one can constrain the overall space–time trend from the high-frequency back-projections.

Overall, the various teleseismic P wave imaging results for a frequency of ~1 Hz for the mainshock resolve a narrow, 150–160 km long zone of unilateral radiation along an azimuth of $110° \pm 10°$ with a rupture expansion velocity of 3.0 ± 0.3 km/s over a duration of 50 to 60 s. Lower frequency imaging indicates a broader zone of energy release extending southward from the ribbon of high-frequency radiation. Details of the associated slip process are not stably resolved. Back-projections for the large aftershock have also been performed, but the images are spatially concentrated and do not provide compelling constraints on the rupture expansion velocity or source dimensions.

4. Finite-fault slip models

The spatial distribution of slip during the 2015 Nepal earthquakes has been analyzed using finite-fault slip model inversions for both kinematic and static slip models. Inversions for the mainshock and aftershock based on only seismological data were rapidly performed by the USGS-NEIC (http://earthquake.usgs.gov/earthquakes/eventpage/us20002926#scientific_finite-fault, as discussed in Hayes et al., 2015), Yagi and Okuwaki (2015), Wang et al. (2015), and several research groups that posted un-reviewed solutions on-line. The NEIC model used a dip of 10° and finds a seismic moment of 8.1×10^{20} Nm (M_W 7.87), with a rupture extending about 110 km along strike with a rupture velocity of about 2.25 km/s. The rapid solution has a very long
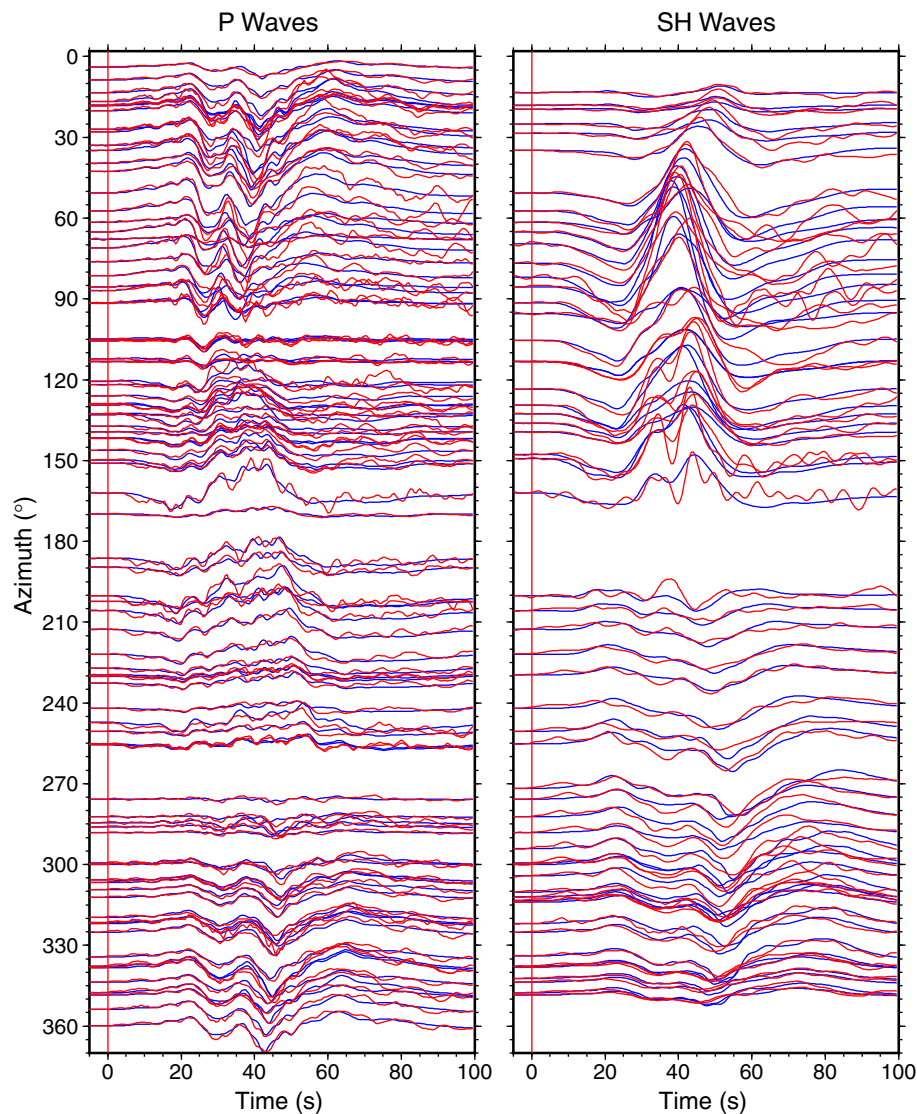
Fig. 7. Observed (red traces) and modeled (blue traces) P wave (left) and SH wave (right) signals for the 2015 mainshock. The synthetics are for the finite-source model in Fig. 6. The signals are plotted with respect to azimuth from the source with true relative amplitudes for P and SH separately. SH amplitudes are all scaled by 0.2 with respect to P. The data are aligned on the first-arrival time. (For interpretation of the references to color in this figure legend, the reader is referred to the web version of this article.)

moment rate function persisting for more than 100 s, which appears to be unreliable as other inversions find rupture durations of no more than 60 s (e.g., Yagi and Okuwaki, 2015; or the SCARDEC solution at http://geoscope.ipgp.fr/index.php/en/catalog/earthquake-description?seis=us20002926), more compatible with the long-period centroid time estimates. Yagi and Okuwaki (2015) imposed a rupture velocity 3 km/s based on their back-projection results, and for a 10° dip, found a 120 km long, 80 km wide rupture with peak slip of 7.5 m centered 50 km east of the epicenter, with seismic moment of 9.1×10^{20} Nm (M_W 7.90).

Several studies have combined seismic and geodetic data to invert for a mainshock slip model, including time-varying high-rate GPS observations, static GPS offsets, and/or InSAR data (e.g., Avouac et al., 2015a; Grandin et al., 2015). Avouac et al. (2015a) find that tight constraints on the up-dip margin of the slip zone are imposed by surface deformations detected by Synthetic Aperture Radar, and they prefer a 140 km long mainshock rupture with slip pulse propagation at 3.0 ± 0.5 km/s, a 50 s duration and total seismic moment of 7.2×10^{20} Nm (M_W 7.84) for 7° dip. Grandin et al. (2015) invert all of the data types for a kinematic rupture with 7° dip with a unilateral rupture velocity of 3.1–3.3 km/s, about a 50–60 s rupture duration, and seismic moment of

7.7×10^{20} Nm (M_W 7.86). A region with slip of 4–7 m extends from 25 km southeast of the epicenter about 80 km along strike and 25 km along dip, giving a high aspect ratio. Back-projection of high-frequency P waves from three networks indicates that the deeper edge of the rupture zone radiates more high frequency, as also inferred by Avouac et al. (2015a).

Inversions of just geodetic data involving local high rate GPS or static GPS and InSAR observations provide further tight constraints on the spatial distribution of slip (e.g., Feng et al. 2015; Galetzka et al., 2015; Hayes et al., 2015; Wang and Fialko, 2015; Zhang et al. 2015). Inversions of just InSAR data lack kinematic information and cannot uniquely determine the fault dip but are consistent with values around 7°, and provide good spatial bounds on the rupture (e.g., Diao et al. 2015; Kobayashi et al., 2015; Lindsey et al., 2015). Slip estimates of 5–6 m in the central region of the rupture are found in these studies.

Given the high quality geodetic constraints and fortunate availability of several high-rate GPS stations straddling the center of the mainshock rupture zone, it is clear that teleseismic data alone cannot provide the optimal finite-fault solution for the mainshock and the large aftershock. For many events teleseismic information is all that is available, and results of teleseismic analysis provide source parameters used to compare
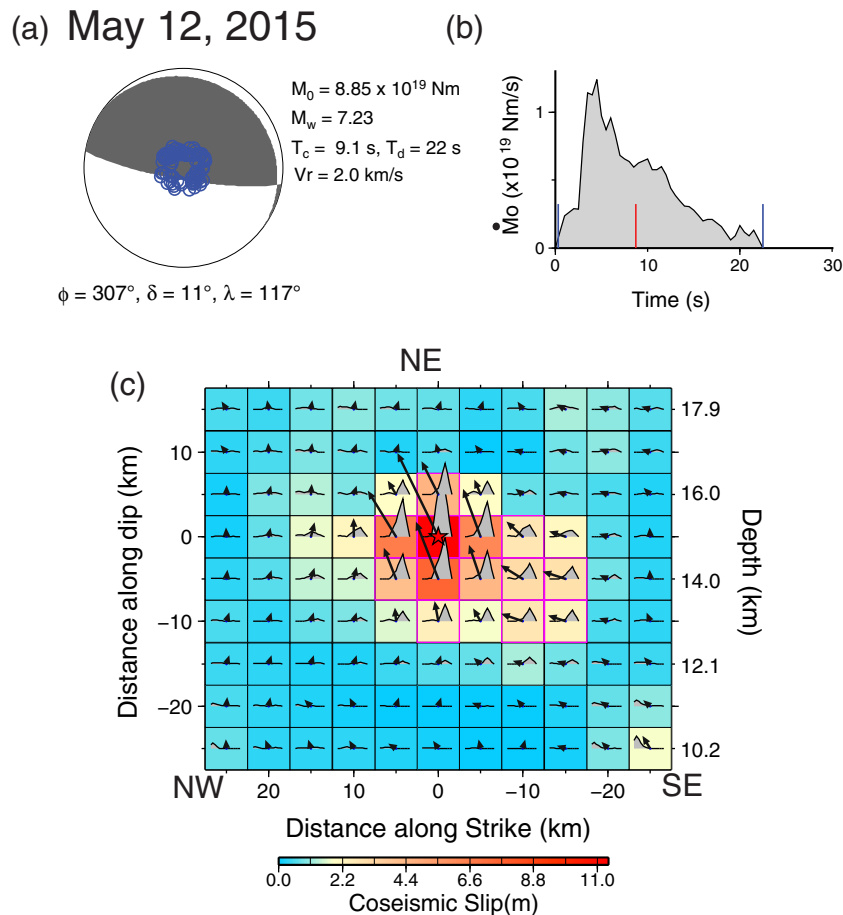
Fig. 8. The finite-fault inversion of teleseismic P and SH waves for the May 12, 2015 event favored in this study. (a) The average focal mechanism of the rupture with the strike, $\phi = 307°$ and dip, $\delta = 11°$ indicates the planar fault geometry. The rake $\lambda = 117°$ is averaged from the variable rake inversion. (b) Moment-rate spectrum for the finite-fault model. The seismic moment was constrained from the gCMT inversion, corresponding $M_W = 7.23$. The centroid time, T_c is indicated by a red tick mark, and the total duration, T_d is bracketed by blue tick marks. (c) Subfault grid with colors and vector lengths indicating slip magnitude and variable subfault average rake direction (vector motion of the footwall (Indian plate) relative to the hanging wall (Eurasian plate)). The subfault moment rate functions are plotted within each cell, with maximum possible durations of 7.5 s. The red star is the hypocenter, at a depth of 15.0 km. This model is shown in map view in Fig. 1. The rupture front expansion velocity $V_r = 2.0$ km/s. (For interpretation of the references to color in this figure legend, the reader is referred to the web version of this article.)

the 2015 events with other earthquakes, so we consider the results of teleseismic-only inversions along with inversions constrained by the geodetic observations. We performed a large number of finite-fault inversions for a range of fault models using a linear least-squares waveform inversion (e.g., Hartzell and Heaton, 1983; Kikuchi and Kanamori, 1991) of 86 teleseismic P and 60 SH wave broadband displacements filtered in the passband 0.005–0.9 Hz. The final near-source 1D velocity structure was adapted from Crust 2.0 (Bassin et al., 2000), although several other near source structures were also tested.

A sampling of finite-fault inversions of the teleseismic data set is shown in Fig. 5, for rupture expansion velocities, $V_r = 2.5$ to 3.3 km/s, grid spacing of 10 to 13.2 km, dip of 7–10°, and hypocentral depths of 8.2 to 15 km. The moment rate functions associated with each model and the basic slip patterns, which have a large-slip zone about 60 km in the negative along-strike direction (ESE), are relatively stable attributes of the solutions. The centroid time estimates, T_c, vary over only a couple of seconds, and are close to the long-period moment tensor centroids, with the total duration of significant seismic wave radiation measured by eye from the moment rate function being about 50 s. Peak slip is not a well-resolved parameter in these models, but varies from 4 to 6 m for solutions that were constrained to have comparable seismic moments. There is a significant degradation in the waveform fit for a hypocenter of 8.2 km, which is the final USGS-NEIC estimate (15 km was the initial value given and many published inversions

used that value). Slip centroid depths tend to be shallower than 15 km if that depth is used for the hypocenter with Crust 2.0 for the source model. The effects of variable source depth within a single source model were as strong or stronger than variations between crustal models, as is commonly found for teleseismic inversions.

The subfault source time functions in these models are parameterized with 4 overlapping 2.5-s rise time triangles, giving possible subfault durations of 12.5 s, bounding the annulus of slip loci to within that time duration after passage of the rupture front. Generally, the subfault source time functions are fairly simple and only in the main slip patch do they use the full slip duration. Deeper subfaults begin to rupture several seconds after the initial rupture front activates the subfault, accommodating a lower effective rupture expansion speed. Exploring long subfault durations and smaller grid spacing does not reveal any distinct characteristics, but the inversions do become poorly resolved in some cases, particularly for fault dip less than 6° and hypocentral depths less than 8 km. This is not unexpected, as the variation in teleseismic Green's functions across the grid reduces as dip and depth decrease, leading to degeneracy in the inversion in that spatial resolution requires sensitivity to variable Green's functions at each time interval. Kinematic constraints certainly impact the solutions, notably the expansion of the slip zone dimensions with increasing rupture velocity, so these models are non-unique, as is always the case. The solutions in Fig. 5 are generally comparable to the published seismological inversions noted above
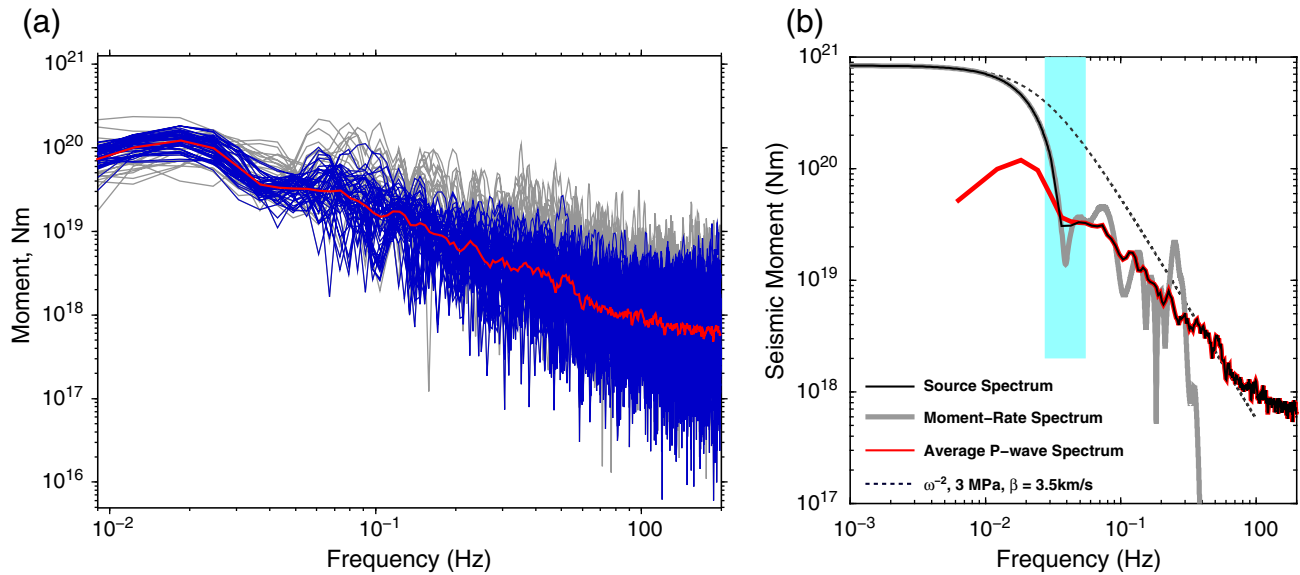
Fig. 9. (a) The mainshock average P wave source spectrum (red curve) estimated by logarithmic averaging of broadband P wave displacement spectra corrected for radiation pattern factors and attenuation (blue curves), omitting stations with radiation pattern factors <0.7 (gray curves). (b) Comparison of the source spectrum from the moment-rate function in Fig. 6b (gray curve) with the average P wave source spectrum (red curve) from (a). The overlap of the spectra at 0.05 Hz (cyan line) indicates that the effects of depth phase interference and source finiteness are comparably estimated by the finite-fault solution and the P spectra averaging. The overall broadband source spectrum estimate (black curve) is the combination of the finite-fault moment-rate spectrum for frequencies less than 0.05 Hz and the average P wave spectrum for frequencies above 0.05 Hz. The dashed curve is for a reference ω-squared spectrum with a stress parameter of 3 MPa and shear velocity of 3.5 km/s.

in having predominantly ESE unilateral rupture expansion, but there are differences in total duration and precise placement of slip along strike.

From the perspective of comparison with the well-resolved geodetic constraints from InSAR observations, the main issue with many of the seismological finite-fault models that we explored is that they tend to distribute slip further up-dip in the main slip patch than indicated by the abrupt edge of slip that produces strong surface offset gradients right through Kathmandu. The geodetic slip models tend to have correspondingly higher aspect ratios, and this is intrinsically difficult to resolve for unconstrained teleseismic models with regularization (spatial smoothing). The up-dip extent of rupture is very important

for evaluating the continuing seismic hazard of the shallowest 50 km of the MHT extending from beneath Kathmandu to the outcrop of the Main Frontal Thrust (MFT, Fig. 1). This issue is simply not well resolved by teleseismic data. We adopt a constraint on the fault dimensions based on up-dip extent of the geodetic models, which have slip extending to about the position of central Kathmandu (Fig. 1, diamond) (e.g., Avouac et al., 2015a; Galetzka et al., 2015; Grandin et al., 2015; Wang and Fialko, 2015). For our estimated upper value of $V_r = 3.3$ km/s from deconvolved back-projections, we obtain the preferred teleseismic rupture model for the mainshock shown in Fig. 6, with corresponding waveform fits in Figs. 7 and S1. The fault geometry and
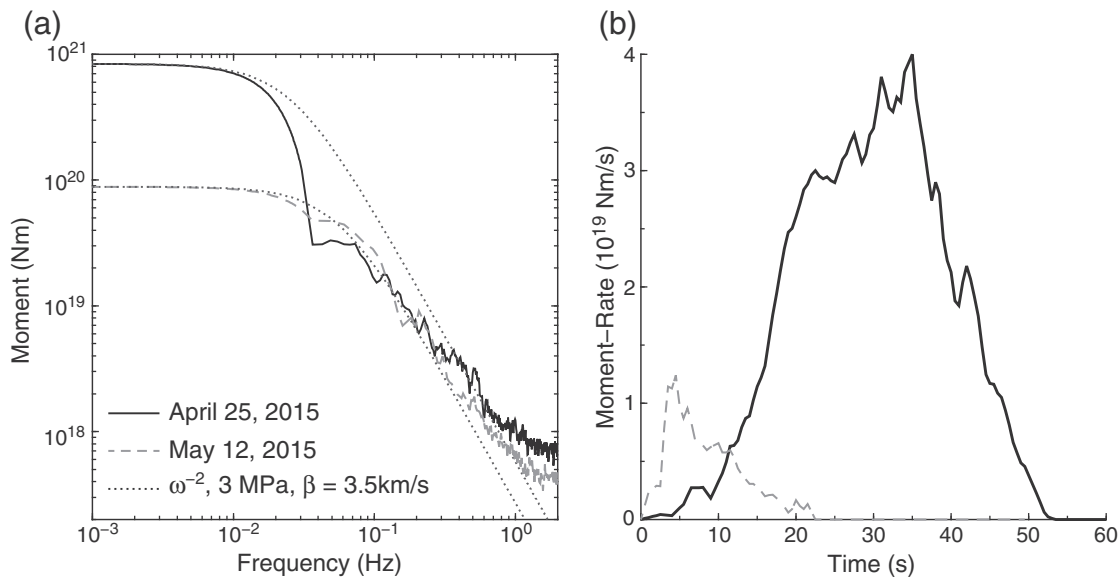

Fig. 10. (a) Direct comparison of the source spectra for the mainshock on April 25, 2015 (black line) and the May 12, 2015 aftershock (dashed gray line). The dotted curves are reference ω-squared spectra with corresponding seismic moments, a stress factor of 3 MPa, and a source shear velocity of β = 3.5 km/s. Despite the difference in long-period moment level, the source radiation is very similar in the frequency band 0.04–0.2 Hz. There is minor relative enrichment of higher frequency radiation for the mainshock. The spectra are reasonably stable to about 1 Hz, but mild flattening at higher frequency may stem from error in the frequency dependent attenuation model or decreasing signal to noise ratio. (b) Direct comparison of the moment rate functions from the finite-fault model inversions for the mainshock (Fig. 6) and the aftershock (Fig. 8).
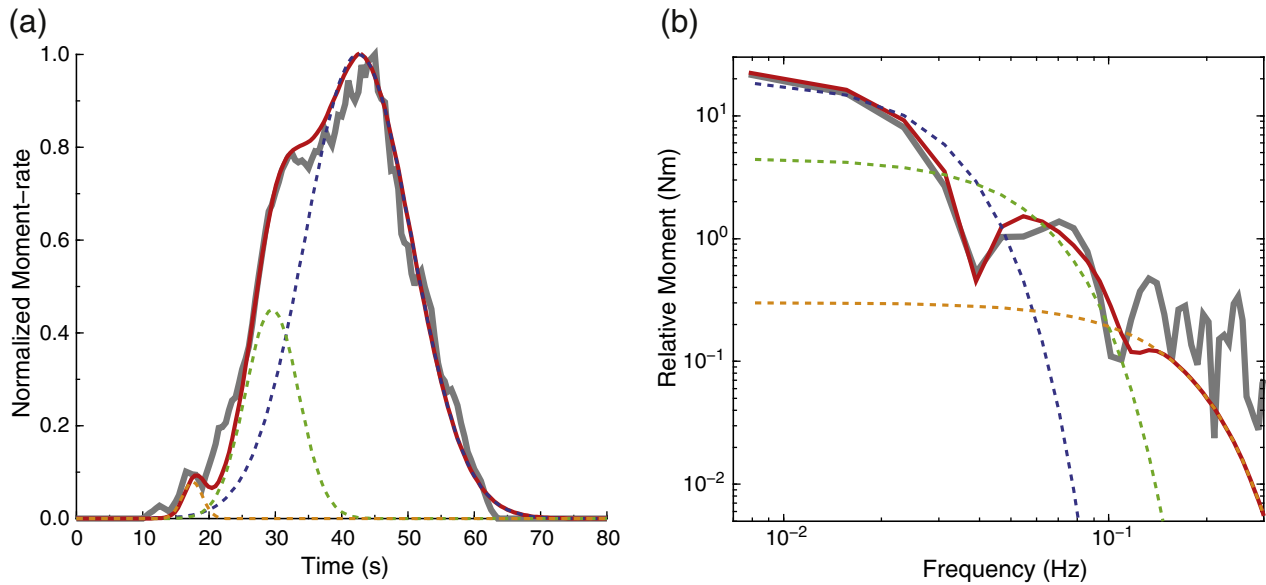
(a)

(b)

Fig. 11. Representation of the moment rate function for the April 25, 2015 mainshock in terms of three Gaussian shaped subevents with variable strengths, durations, and timing. (a) The observed moment rate function is shown in gray, with normalized amplitude, and a sequence of three Gaussian function subevents is shown in yellow, green and blue, with composite form in red, approximately matching the overall shape of the observed moment rate function. (b) Amplitude spectra of the moment rate function and subevents in (a) with corresponding color-coding. The composite spectrum for the three Gaussian subevents acquires the deep scallop near 0.04 Hz like that observed for the observed moment rate spectrum. (For interpretation of the references to color in this figure legend, the reader is referred to the web version of this article.)

seismic moment are constrained to the gCMT point-source best double-couple values, with the hypocentral depth set at 11.8 km based on comparisons with the structural model of Wang and Fialko (2015). The main slip patch has peak slip values of about 7.4 m 65 km SE of the hypocenter (Fig. 6c), and there is a down-dip patch of slip about 80 km from the hypocenter. The latter feature is apparent in most of the geodetic surface motions and inversions, although it is usually ~10 km further east. It locates near the estimated epicenter of the 1833 earthquake (Fig. 1). Rake was allowed to vary within 45° of the average gCMT best-double couple rake of 96° in this model. The variation in rake seen in Fig. 6 is not well-resolved; if rake variation is minimized, the residual waveform mismatch increases by about 2% but the basic pattern of slip remains stable (Fig. S2). The abrupt up-dip termination of slip in the model in Fig. 6 (the only constraint imposed by the geodetic solutions) would normally prompt expansion of the model grid, leading to shallower distribution of slip (as seen in the middle row of Fig. 5), but no other major difference in the solution for these kinematic parameters.

Finite-source models for the May 12, 2015 aftershock based on teleseismic waves alone also have some limitations in their resolution, but these stem primarily from lack of significant spatial directivity in the rupture process (a common issue for moderate size ruptures). Using the faulting geometry and seismic moment from the gCMT best-double couple, and the USGS-NEIC hypocentral depth of 15 km, we obtain the slip model shown in Fig. 8 using a rupture velocity of 2.0 km/s. This model fits over 90% of the power in the 97 broadband P waveforms used in the inversion (Figs. S3, S4). The simple character of the waveforms accounts for the simple rupture model. The moment rate function rises rapidly and then trails off over ~22 s duration, which is a stable characterization of the source process. The gradual drop off of the moment rate-functions limits generation of waveform features that would help to resolve any directivity. The peak slip in the model is about 11.5 m, but this value is very dependent upon the assumed grid spacing and rupture velocity, neither of which is well-resolved. The spatial pattern of our model compares well with the on-line finite-fault solution of the USGS-NEIC (Hayes et al., 2015), although that model again has a long duration tail of the moment rate function extending to 40 s which we do not find evidence for in the observed waveforms. Our

average moment rate function is similar to that of the SCARDEC solution (http://geoscope.ipgp.fr/index.php/en/catalog/earthquake-description?seis=us20002ejl).

The teleseismic finite-fault slip model parameters for both large Nepal earthquakes have well-resolved moment rate functions and stable first-order slip distributions relative to the determinations with local hr.-GPS and other geodetic data, but they are limited in spatial resolution, particularly for the up-dip limit of slip for the mainshock and the radial extent of the aftershock. Recognizing these limitations, we proceed to consider several important teleseismic source parameters for both events.

5. Source spectra and stress drop estimates

Far-field source spectra for the 2015 mainshock and aftershock are determined by combining the <0.05 Hz spectra of the moment-rate functions for the preferred finite-source models in Figs. 6c and 8c, with logarithmically averaged broadband P wave spectra for frequencies above 0.05 Hz. The individual P wave spectra are corrected for geometric spreading, radiation pattern factors that account for up- and down-going phases, and frequency-dependent attenuation, t* (f) (where t* is the path integral of P velocity divided by the P wave quality factor Q(f)). This procedure is demonstrated for the mainshock in Fig. 9. Fig. 9a illustrates that the average P wave spectrum is stable with the large number of observations, after omitting stations with radiation pattern factors less than 0.7. Fig. 9b shows that the spectrum of the finite-fault solution overlaps with that of the average P wave spectrum at 0.05 Hz, where the cross-band spectrum is computed. Depth phase and source finiteness effects are rigorously accounted for in the low frequency part of the spectrum, but only approximately in the high frequency part of the spectrum. However, the agreement at 0.05 Hz indicates that there is no significant bias in the spectral levels of the averaged P wave-spectra, mainly due to the extensive averaging involved.

The average source spectra for the mainshock and aftershock are directly compared in Fig. 10a along with reference spectra for a simple ω-squared "Brune" model with a stress factor of 3 MPa and a source shear velocity of 3.5 km/s and seismic moments corresponding to the gCMT
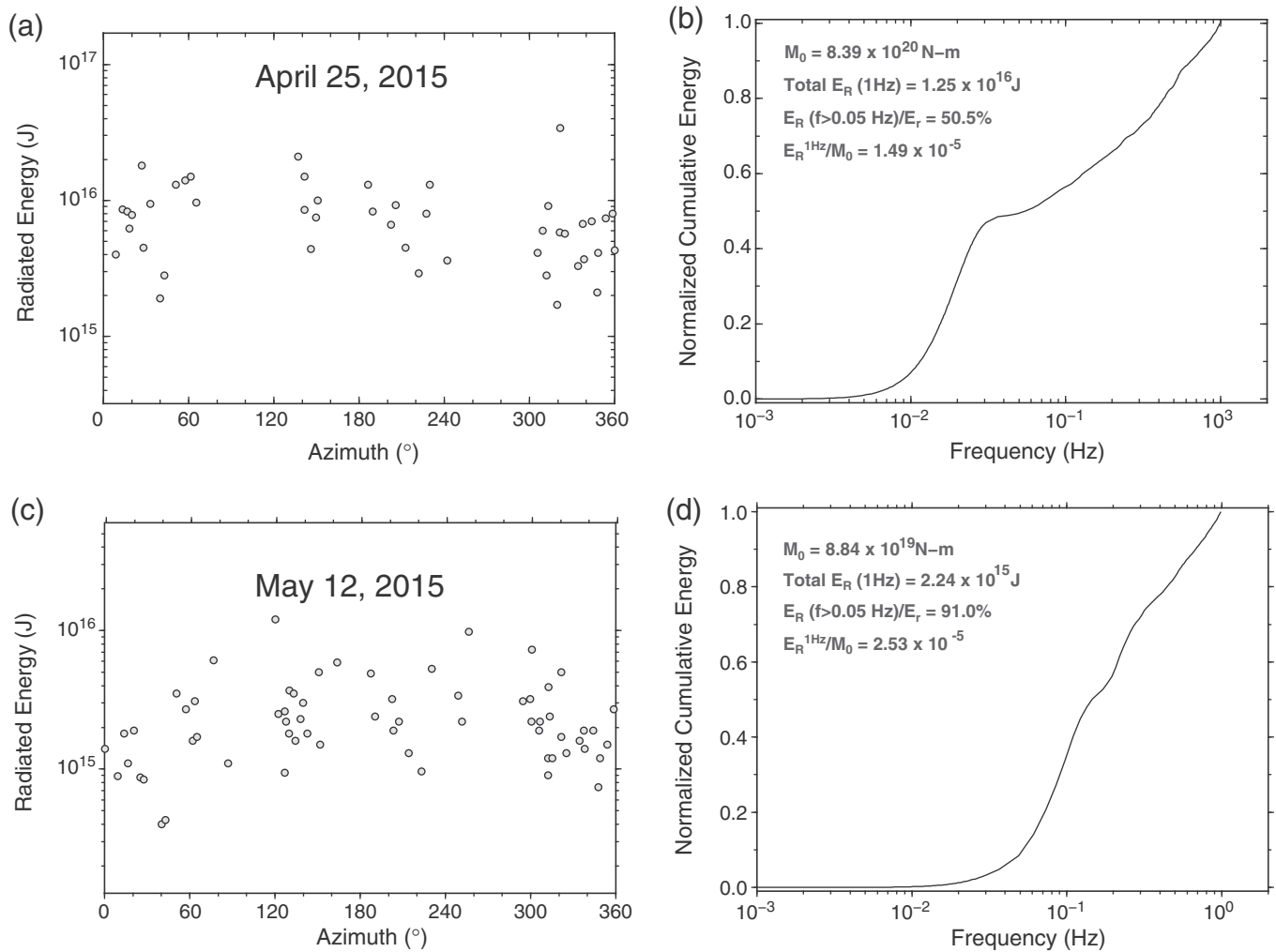
Fig. 12. (a) Single-station estimates of radiated energy, E_R, from broadband P waves for the mainshock plotted versus azimuth. The average value is 6.34×10^{15} J. (b) Cumulative relative energy versus frequency for the mainshock. The seismic moment, total radiated energy up to 1 Hz, fraction of the total radiated energy above 0.05 Hz, and moment-scaled radiated energy are indicated. (c) Single-station estimates of radiated energy, E_R, from broadband P waves for the aftershock plotted versus azimuth. (d) Cumulative relative energy versus frequency for the aftershock. The seismic moment, total radiated energy up to 1 Hz, fraction of the total radiated energy above 0.05 Hz, and moment-scaled radiated energy are indicated.

values. While the theoretical spectra for the two events have significant differences between 0.02 and 1.0 Hz, the measured spectra overlap between 0.03 and 1.0 Hz. This is particularly interesting given the large differences in the moment-rate functions (Fig. 10b). The mainshock spectrum is observed to have a steep notch around 0.035 Hz, and both spectra fall off somewhat less gradually than the ω-squared model out to 1 Hz. There is an indication of flattening of the spectra above 1 Hz, suggestive of either incorrect average $t^*(f)$ or low signal-to-noise ratio. A single model for $t^*(f)$ from Pérez-Campos et al. (2003) is used for all paths, which is an obvious over-simplification. If we use an alternate model for $t^*(f)$ with stronger frequency dependence such as that given by Choy and Cormier (1986), the spectra fall off more linearly above 1 Hz, but the spectral overlap remains.

The source spectra in Fig. 10a differ significantly from those presented by Denolle et al. (2015). They assume a parameterized reference source spectrum, modify it to account for point source depth phase interference and attenuation, and fit observed P wave spectra to obtain the average far-field P spectrum. They predict spectral levels for the mainshock of about 9×10^{19} Nm at 0.1 Hz, whereas our direct measurements are a factor of 3 to 5 lower in the corresponding frequency range. Their models also predict systematically higher spectral levels for the mainshock relative to the aftershock out to 2 Hz. Our spectra are directly measured across the entire band and do not depend on an assumed

form of the overall spectrum. Furthermore, the observed local ground accelerations for the mainshock in Kathmandu are less than a factor of two larger than those for the aftershock despite longer pathlengths for the latter (e.g., Bhattarai et al., 2015). Also the aftershock appears to locate on the deeper portion of the MHT, along the swath of high frequency radiation for the mainshock. The relatively low $m_b = 7.1$ for the mainshock relative to 6.8 for the aftershock is consistent with our mainshock depleted high-frequency spectrum, although magnitude saturation is an issue for the larger event.

The deep spectral scalloping for the mainshock appears to be a manifestation of smooth rupture of the main portion of the fault. We explore this problem by fitting three Gaussian-shaped functions to the moment-rate function of the mainshock (Fig. 11a), and computing the spectrum of each Gaussian function. These spectra have smooth Gaussian shape in the frequency domain with spectral roll-offs much faster than the ω-squared spectrum, so we explore them as parameterizations of very smooth portions of the rupture. Then we compute a composite moment-rate function by summing the 3 Gaussian moment-rate functions (red curve in Fig. 11a). The moment-rate spectrum of the composite moment-rate function, shown in red in Fig. 11b, yields a deep trough near 0.04 Hz similar to the observed spectrum. We infer that the smooth slip distribution in the main slip pulse region of the model in Fig. 6c, with spatially distributed growth and termination of slip along strike,
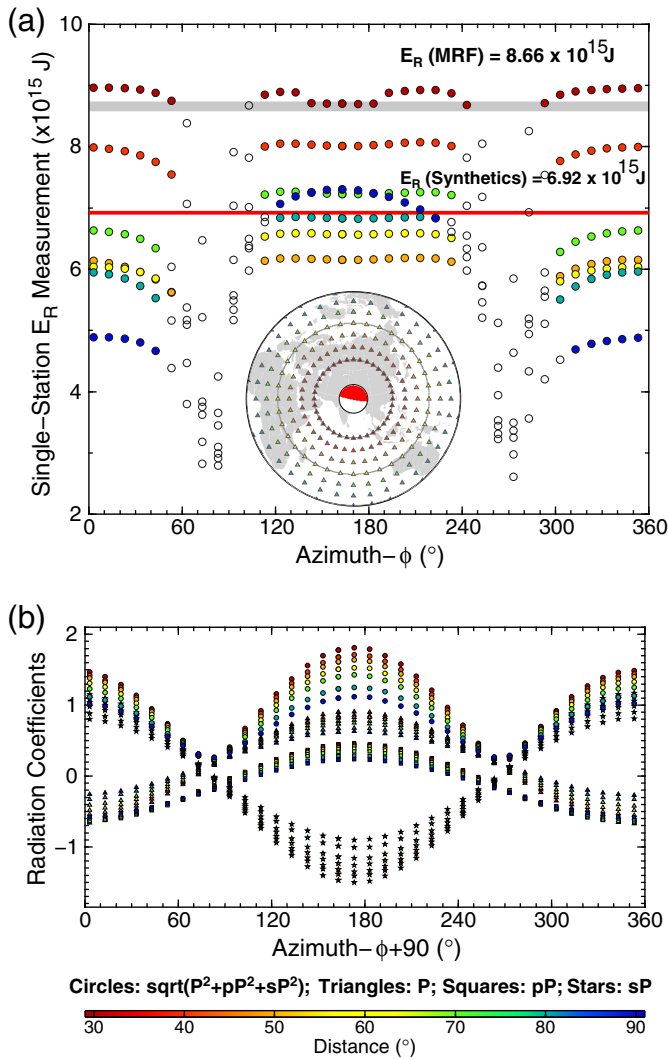
Fig. 13. (a) Single station measurements of radiated energy, E_R, from P wave synthetics for the mainshock finite-source model in Fig. 6 at uniformly sampled azimuths and distances ranging from 30° to 90° (color-coding and inset map distribution). Empty circles are those cases for which the radiation coefficient factor (shown by circles in (b)) is less than 0.7; these values are excluded in computing the mean E_R of 6.92×10^{15} J, which is within 20% of the actual value computed for the mainshock moment rate function of 8.66×10^{15} J. (b) The azimuthal and distance values of radiation pattern coefficients for P, pP and sP, along with the combined radiation coefficient. (For interpretation of the references to color in this figure legend, the reader is referred to the web version of this article.)

produces the smooth Gaussian-like moment-rate function with rapid spectral fall-off which reflects the relatively uniform stress release over the planar, shallow dipping fault surface. The spectrum does not fall off as rapidly at high frequency, so it appears to be associated with more typical rupture characteristics.

We compute radiated energy, E_R, for the mainshock and aftershock using far-field P wave ground velocity observations and the method of Venkataraman and Kanamori (2004), augmented by the calculated contribution for the low frequency (<0.05 Hz) part of the moment-rate spectrum (Fig. 12). We estimate the radiated energy up to 1 Hz, avoiding contributions from the flattening portions of our attenuation-corrected spectra. For our preferred rupture model for the mainshock we obtain $E_R = 1.25 \times 10^{16}$ J (50.6%, or 6.34×10^{16} J, of this E_R estimate is from single station estimates for frequencies above 0.05 Hz as apparent in Fig. 12b), and a moment-scaled value $E_R/M_0 = 1.49 \times 10^{-5}$ (Fig. 12b). This E_R estimate fluctuates by about 20% among the large suite of source models we considered, but has additional uncertainty

associated with the specific attenuation model and the choice of relative contribution of P and S energy to the total (we use dislocation theory for which the P and S source spectra have the same corner frequency). The broadband energy estimate for the mainshock produced by IRIS (http://ds.iris.edu/spud/eqenergy/9925797) using the method of Convers and Newman (2011) is 7.3×10^{15} J, an estimate that does not fully account for the low frequency contributions that we include. In contrast, the high spectral amplitudes estimated by Denolle et al. (2015) yield a high estimate of E_R of 5.87×10^{16} J.

Differences in radiated energy estimation by different investigators are commonly observed, due primarily to variation in attenuation assumptions, methods for radiation pattern corrections, and assumed relative contribution of (not directly measured) S wave energy. Fig. 13 explores the issue of radiation pattern corrections for the mainshock, which has substantial azimuthal waveform variations (Fig. 7), and substantial directivity. We examine how appropriate our procedure is using synthetic P waves computed for regularly sampled distances and azimuths. The time history of the source is given by the moment-rate function shown in Fig. 6. Then, we make single-station estimates of E_R in exactly the same way as we do for the Nepal earthquake. Fig.13a shows the results with the average of E_R computed from those signals with stable radiation factors greater than 0.7 (the radiation factor is the square root of the sum of the squares of the phase amplitudes for
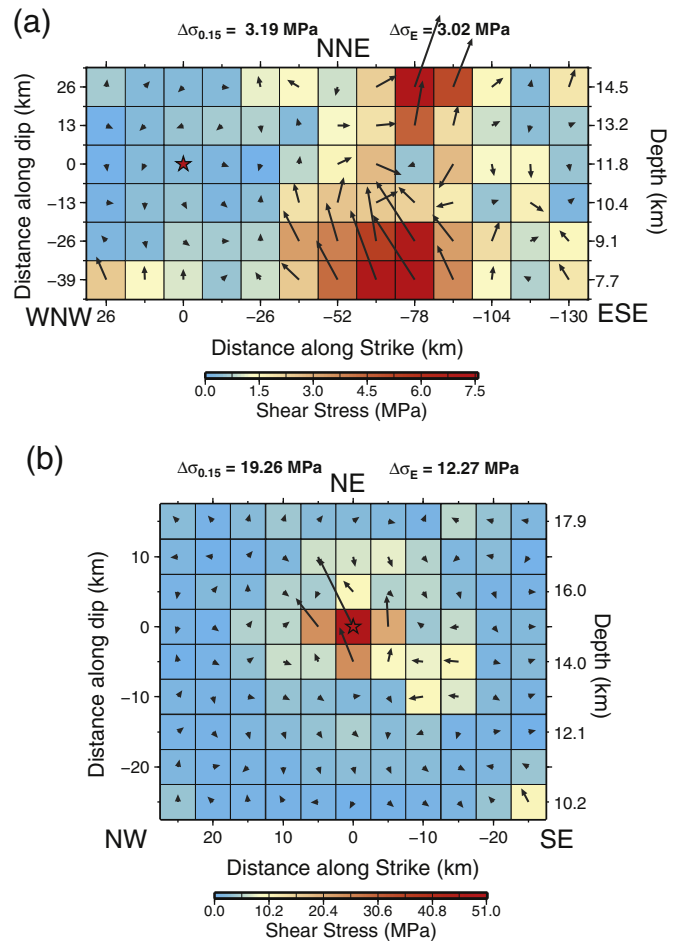

Fig. 14. Stress drop estimation for (a) the April 25, 2015 mainshock and (b) the May 12, 2015 aftershock based on the finite-fault inversions in Figs. 6 and 8. The shear stress associated with the average dislocation on each subfault (footwall side) is computed for a half-space model at the center of the subfault. The magnitude and direction of the computed shear stresses are indicated by the color palette and vectors. The red stars are the hypocenter locations. The static stress drop estimates $\Delta\sigma_{0.15}$ and $\Delta\sigma_E$ discussed in the text are computed for each event. (For interpretation of the references to color in this figure legend, the reader is referred to the web version of this article.)
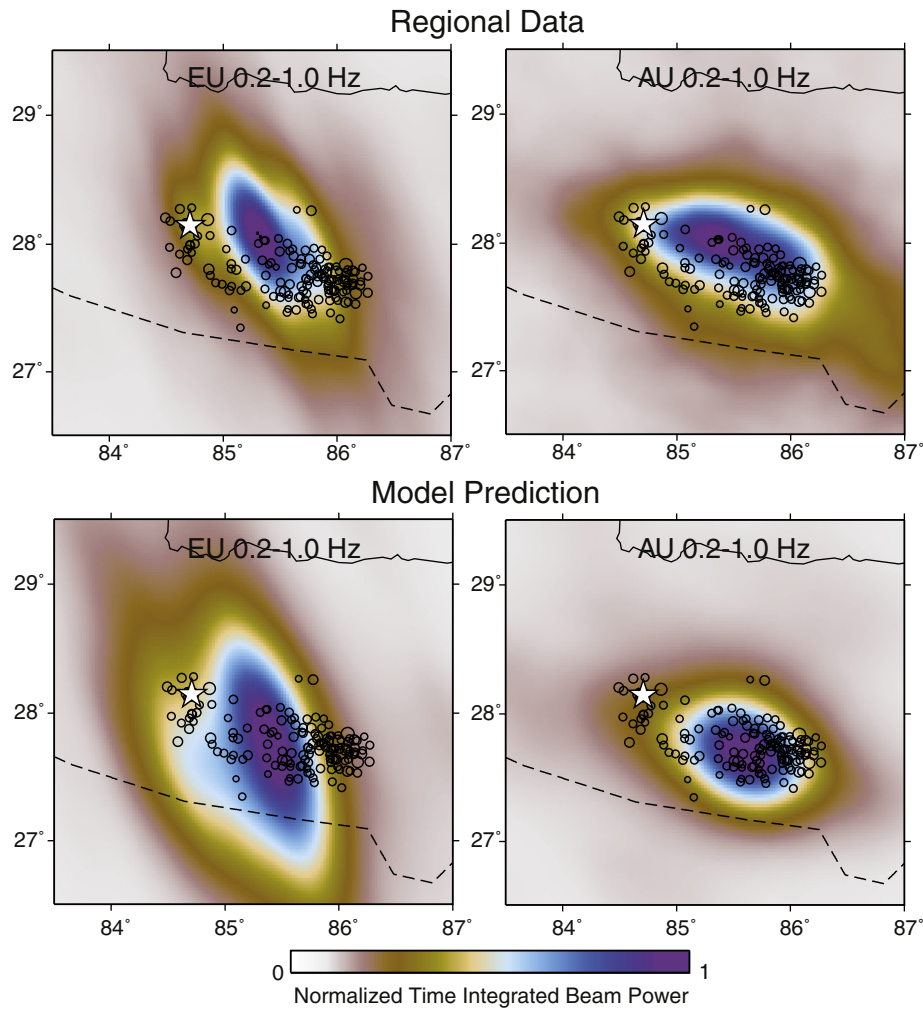
Fig. 15. Time-integrated images of back-projection of P wave data and synthetics for the finite fault model for the April 25, 2015 mainshock (Fig. 6) for a passband of 0.2–1.0 Hz for regional networks in Europe (EU) and Australia (AU). The one-month aftershock locations are superimposed on the images. Each image is influenced by the specific network response function, which is shared by the data and model images. The source model tends to shift the centroid of the back-projected beam power slightly to the south of the data images, indicating that the finite-fault model is not capturing the shortest period radiation precisely. This supports the likelihood that the down-dip portion of the fault radiated relatively enriched short-period energy.

P, pP and sP, which includes the free surface reflection effects). The average, 6.92×10^{15} J, is about 20% less than the value directly computed from the moment rate function shown in Fig. 6, which gives 8.66×10^{15} J. Fig. 13b shows the radiation coefficients used for computing the single-station estimates. This test demonstrates that the depth phase effects on the E_R estimation are approximately accounted for, and suggests that the uncertainty in our estimate of the radiated energy for the Nepal earthquake is comparable.

For the aftershock our estimate is $E_R = 2.24 \times 10^{15}$ J, and $E_R/M_0 = 2.53 \times 10^{-5}$ (Fig. 12d). The broadband radiated energy estimated for this event from IRIS (http://ds.iris.edu/spud/eqenergy/9954452) is 1.9×10^{15} J. The low frequency (<0.05 Hz) contribution is only about 9% for this event, so our estimate is not much larger than that from IRIS. The estimate from Denolle et al. (2015) is 4.11×10^{15} J, again high compared to the other estimates.

While imperfectly resolved, the finite-fault models for the mainshock and aftershock provide variable slip distributions over specific rupture areas that we can use to estimate the static stress drop. We apply two approaches; a simplified procedure is to suppress the poorly resolved low slip portions of the models by retaining only those subfaults for which the subfault total moment is larger than 15%

of the peak subfault total moment, then use the average slip over the cumulative remaining subfault area in a circular crack model to estimate stress drop, $\Delta\sigma_{0.15}$. The 15% value is typical of values used to trim poorly resolved portions of finite-fault models (see Ye et al., 2016). This gives estimates for the mainshock of $\Delta\sigma_{0.15} = 3.2$ MPa and for the aftershock $\Delta\sigma_{0.15} = 19.3$ MPa. A preferred alternate approach, illustrated in Fig. 14, is to calculate the dislocation induced shear stress at the center of each grid point in the model for the variable slip distribution and to then calculate the slip-weighted average shear stress drop, $\Delta\sigma_E$, over the fault surface using the procedure of Noda et al. (2013). This gives estimates of $\Delta\sigma_E = 3.0$ MPa for the mainshock and $\Delta\sigma_E = 12.3$ MPa for the aftershock. The formal uncertainty is hard to assess as the models have many parameters and undoubtedly are smoothed versions of true slip heterogeneity, but within the range of model parameters explored and for the grid sizes used, we estimate at least a factor of 2 uncertainty up or down (range of factor of 4) based on analysis of kinematic inversions for many events (Ye et al., 2016). For example, if we consider a slip model with very little rake variation allowed, we find $\Delta\sigma_E = 3.01$ MPa for the mainshock (Fig. S2), and overall variations in estimates well within the estimated factor of 2 uncertainty. Denolle et al. (2015) assume a circular crack model and their spectral characteristics to estimate stress
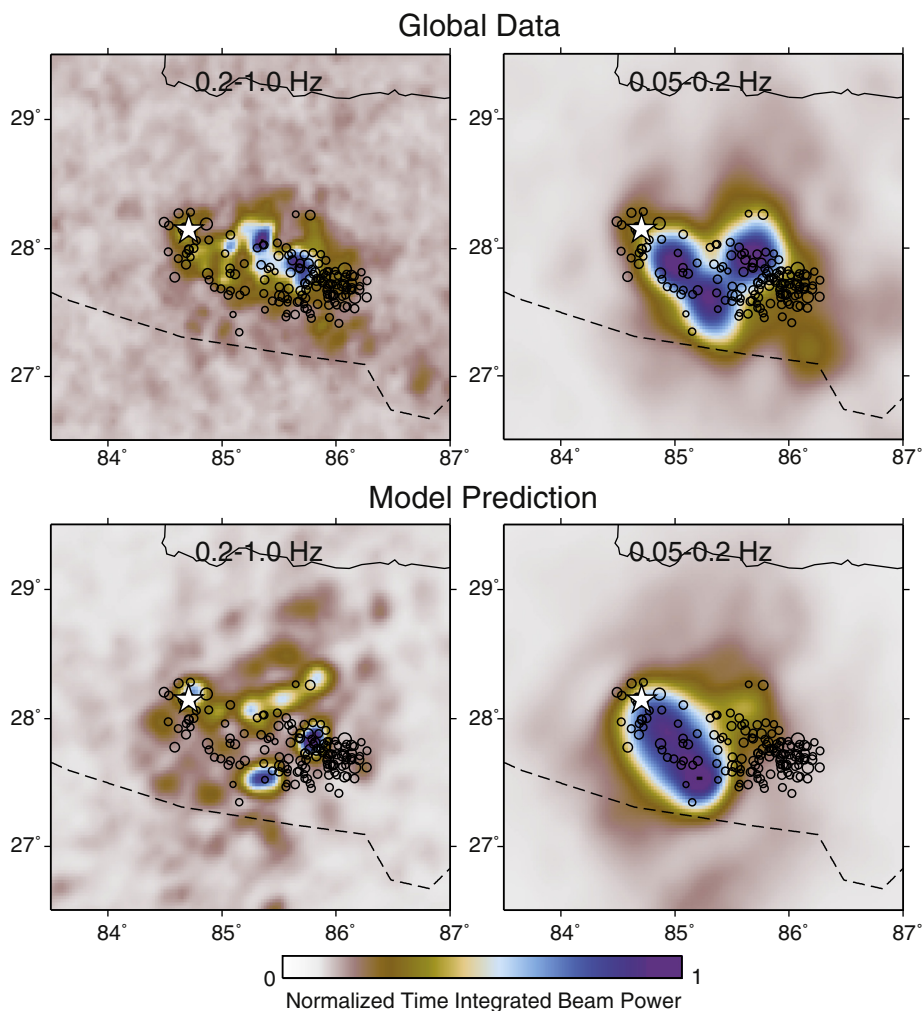
Global Data

Fig. 16. Time-integrated images of back-projection of P wave data and synthetics for the finite fault model for the April 25, 2015 mainshock (Fig. 6) for passbands of 0.2–1.0 Hz and 0.05–0.2 Hz for the global station distribution. The one-month aftershock locations are superimposed on the images. The longer-period data images suggest some coherent energy originating south of the high frequency images. This is largely reproduced by the finite-source model at lower frequency, but the high frequency image has limited agreement with the data.

drops of 22.7 ± 1.9 MPa and 20.2 ± 1.3 MPa for the mainshock and aftershock, respectively. Those results are highly model dependent and have unrealistically small uncertainty estimates.

6. Comparison of back-projections for data and finite-fault synthetics

A consistent feature of the teleseismic and near-field rupture analyses is that coherent bursts of high-frequency radiation appear to originate in the deeper portion of the rupture zone, with the space–time history appearing to track the slip-rate front (e.g., Avouac et al., 2015a; Galetzka et al., 2015; Grandin et al., 2015; Yagi and Okuwaki, 2015). The distance from this deep radiation may have played a role in limiting its contribution to damage in Kathmandu. Our back-projection and finite-fault inversions support the contention that there is distinct behavior of the radiation along dip. In Fig. 15 we compare time-integrated back-projected beam power for two regional arrays for the period range 0.2 to 1.0 Hz for data and for synthetics from the finite-fault model in Fig. 6c. The data images show distributed power along the down-dip region of the aftershock zones, consistent with the observations noted above (the tendency strengthens at higher frequencies, but the finite-source models do not recover frequencies higher than about 0.5 Hz at best, so we use a relatively low frequency passband). The back-projections of the model synthetics show modest,

but systematic southward shifts of the imaged sources of radiation, centered more on the aftershock zone. The frequency dependence is even more pronounced for global back-projections of data and finite-faulting synthetics, as shown in Fig. 16. Here the time integrated back-projections agree well with the major features noted by Fan and Shearer (2015) for corresponding passbands, while the images formed from the corresponding finite-fault synthetics match the basic up-dip (southerly) shift of the 0.05–0.2 Hz radiation while only partially capturing the down-dip lineation of radiation. The teleseismic data thus indicate that the variable ground shaking around the source region may be a combined effect of relatively smooth slip beneath northern Kathmandu and down-dip bursts of high-frequency radiation along the belt of back-ground microseismicity north of the city.

7. Discussion and conclusions

Estimation of teleseismic source parameters for large earthquakes is an essential undertaking for rapid assessment of faulting and societal impact of earthquakes, for providing a basis to compare events with earlier activity in a region, and for seismotectonic applications. The 2015 Nepal earthquakes had substantial catastrophic impact, but the entire Himalayan front continues to have potential for future major and great earthquakes. An important aspect of the mainshock rupture is that slip did not extend up to the surface, and in fact there is about a

50 km up-dip width along the MHT and MFT splay that continues to have slip-deficit that is not being released in after-slip (Avouac et al., 2015b). This is very hard to demonstrate by teleseismic analysis alone, but is well established by geodetic and field observations. The teleseismic analyses, in contrast, provide good characterization of the space–time history of the rupture, the average and variable slip distribution, the total energy release, the average stress drop on the fault, and the fault dip. Thus, source parameter estimation with teleseismic data, both without and with modest constraints from the geodetic observations, provides a useful means for both rapid event analysis and refined parameter estimation as in this study, subject to the limitations intrinsic to teleseismic studies (most of which are well recognized by practitioners, but not always by other users of the seismological parameters).

Back-projection methods provide valuable information about high-frequency rupture expansion and temporal duration, but even the methods designed to suppress artifacts from depth phases, array response, and slowness errors, do not give a unique image of specific space–time features producing high-frequency radiation. This may be a result of directionality of the radiation from the complex faulting. The frequency dependence of radiation as a function of source depth for the Nepal events is similar to that found for megathrust subduction zone faults, but the interpretation of bounding ramps and local changes in dip invoked for the Nepal MHT (e.g., Avouac et al., 2015a; Galetzka et al., 2015; Grandin et al., 2015) may be distinct from the deeper wedge structure along megathrusts, which are generally not characterized by such narrow distributions of background small earthquake activity. The frequency-dependence in back-projections supports the distinctions between the finite-fault slip models with large slip in the shallower portion of the rupture zone where there is less background activity, but significant aftershock activity. Radiated energy and stress drop estimates for the mainshock are within the conventional range of parameters for interplate earthquakes, while the aftershock stress drop appears to be higher. The overall source spectra of the mainshock and aftershock overlap significantly for mid-range frequencies from 0.03 to 1.0 Hz, which may account for similarity in peak ground motions in this passband at comparable distances. We believe that this spectral feature is robustly resolved from teleseismic analysis. Although the best overall characterization of these source attributes can be achieved by integration of all information into joint models, refined teleseismic modeling will remain important for characterization of earthquakes.

Supplementary data to this article can be found online at http://dx.doi.org/10.1016/j.tecto.2016.05.023.

Acknowledgments

References

Ader, T., Avouac, J.-P., Liu-Zeng, J., Lyon-Caen, H., Bollinger, L., Galetzka, J., et al., 2012. Convergence rate across the Nepal Himalaya and interseismic coupling on the Main Himalayan Thrust: implications for seismic hazard. J. Geophys. Res. 117, B04403.

Adhikari, L.B., Gautam, U.P., Koirala, B.P., Bhattarai, M., Kandel, T., Gupta, R.M., et al., 2015. The aftershock sequence of the 2015 April 25 Gorkha-Nepal earthquake. Geophys. J. Int. 203, 2119–2124. http://dx.doi.org/10.1093/gji/ggv412.

Angster, S., Fielding, E.J., Wesnousky, S., Pierce, I., Chamlagain, D., Gautam, D., Upreti, B.N., Kumahara, Y., Nakata, T., 2015. Field reconnaissance after the 25 April 2015 M 7.8 Gorkha earthquake. Seismol. Res. Lett. 86 (6), 1506–1513. http://dx.doi.org/10.1785/0220150135.

Avouac, J.-P., Meng, L., Wei, S., Wang, T., Ampuero, J.-P., 2015a. Lower edge of locked Main Himalayan Thrust unzipped by the 2015 Gorkha earthquake. Nat. Geosci. 8 (9), 708–711. http://dx.doi.org/10.1038/NGEO2518.

Avouac, J.-P., Meng, L., Melgar, D., Wei, S., Wang, T., Bock, Y., Ampuero, J.-P., Stevens, V., Galetzka, J., Genrich, J., 2015b. Unzipping of the locked MHT by the 2015, M_W 7.8 Gorkha earthquake, Nepal. Geological Society America (Meeting Abstracts 105-2, 2015 Baltimore Meeting).

Bai, L., Liu, H., Ritsema, J., Mori, J., Zhang, T., 2016. Faulting structure above the Main Himalayan Thrust as shown by relocated aftershocks of the 2015 M_W 7.8 Gorkha, Nepal earthquake. Geophys. Res. Lett. 43 (2), 637–642. http://dx.doi.org/10.1002/2015GL066473.

Bassin, C., Laske, G., Masters, G., 2000. The current limits of resolution for surface wave tomography in North America. EOS Trans AGU 81, F897.

Bhattarai, M., Adhikari, L.B., Gautam, U.P., Laurendeau, A., Labonne, C., Hoste-Colomer, R., Sébe, O., Hernandez, B., 2015. Overview of the large 25 April 2015 Gorkha, Nepal, earthquake from accelerometric perspectives. Seismol. Res. Lett. 86 (6), 1540–1548.

Bilham, R., 1995. Location and magnitude of the 1833 Nepal earthquake and its relation to the rupture zones of contiguous great Himalayan earthquakes. Curr. Sci. 69, 101–128.

Bilham, R., 2015. Raising Kathmandu. Nat. Geosci. 8, 582–584.

Bilham, R., Ambraseys, N., 1995. Apparent Himalayan slip deficit from the summation of seismic moments for Himalayan earthquakes, 1500–2000. Curr. Sci. 88, 1658–1663.

Bilham, R., Gaur, V.K., Molnar, P., 2001. Himalayan seismic hazard. Science 293, 1442–1444.

Bollinger, L., Sapkota, S.N., Tapponnier, P., Klinger, Y., Rizza, M., Van der Woerd, J., Tiwari, D.R., Pandey, R., Bitri, A., Bes de Berc, S., 2014. Estimating the return times of great Himalayan earthquakes in eastern Nepal: evidence from the Patu and Bardib as strands of the Main Frontal Thrust. J. Geophys. Res. Solid Earth 119. http://dx.doi.org/10.1002/2014JB010970.

Bollinger, L., Tapponnier, P., Sapkota, S.N., Klinger, Y., 2016. Slip Deficit in Central Nepal: Omen for a Pending Repeat of the 1344 AD Earthquake (Nature Communications). (in press).

Choy, G.L., Cormier, V.F., 1986. Direct measurement of the mantle attenuation operator from broadband P and S waveforms. J. Geophys. Res. 91, 7326–7342.

Convers, J.A., Newman, A.V., 2011. Global evaluation of large earthquake energy from 1997 through mid-2010. J. Geophys. Res. 116, B08304. http://dx.doi.org/10.1029/2010JB007928.

Denolle, M.A., Fan, W., Shearer, P.M., 2015. Dynamics of the 2015 M7.8 Nepal earthquake. Geophys. Res. Lett. 42, 7467–7475. http://dx.doi.org/10.1002/2015GL065336.

Diao, F., Walter, T.R., Motagh, M., Prats-Iraola, P., Wang, R., 2015. The 2015 Gorkha earthquake investigated from radar satellites: slip and stress modeling along the MHT. Frontiers in Earth Science 3, 65. http://dx.doi.org/10.3389/feart.2015.00065.

Dixit, A.M., Ringler, A.T., Sumy, D.F., Cochran, E.S., Hough, S.E., Martin, S.S., et al., 2015. Strong-motion observations of the M 7.8 Gorkha, Nepal, earthquake sequence and development of the N-SHAKE strong-motion network. Seismol. Res. Lett. 86 (6), 1533–1539. http://dx.doi.org/10.1785/0220150146.

Duputel, Z., Rivera, L., Kanamori, H., Hayes, G., 2012. W phase source inversion for moderate to large earthquakes (1990–2010). Geophys. J. Int. 189, 1125–1147. http://dx.doi.org/10.1111/j.1365-246X.2012.05419.x.

Duputel, Z., Tsai, V.C., Rivera, L., Kanamori, H., 2013. Using centroid time-delays to characterize source durations and identify earthquakes with unique characteristics. Earth Planet. Sci. Lett. 375, 92–100. http://dx.doi.org/10.1016/j.epsl.2013.05.024.

Duputel, Z., Vergne, J., Rivera, L., Wittlinger, G., Farra, V., Hetényi, G., 2016. The 2015 Gorkha earthquake: a large event illuminating the Main Himalayan Thrust fault. Geophys. Res. Lett. 43. http://dx.doi.org/10.1002/2016GL068083.

Fan, W., Shearer, P.M., 2015. Detailed rupture imaging of the 25 April 2015 Nepal earthquake using teleseismic P waves. Geophys. Res. Lett. 42, 5744–5752. http://dx.doi.org/10.1002/2015GL064587.

Feng, G., Li, Z., Shan, X., Zhang, L., Zhang, G., Zhu, J., 2015. Geodetic model of the 2015 April 25 M_W 7.8 Gorkha Nepal earthquake and M_W 7.3 aftershock estimated from InSAR and GPS data. Geophys. J. Int. 203, 896–900. http://dx.doi.org/10.1093/gji/ggv335.

Galetzka, J., Melgar, D., Genrich, J.G., Geng, J., Owen, S., Lindsey, E.O., et al., 2015. Slip pulse and resonance of the Kathmandu basin during the 2015 Gorkha earthquake, Nepal. Science 349, 1091–1095. http://dx.doi.org/10.1126/science.aac6383.

Goda, K., Kiyota, T., Pokhrel, R.M., Chiaro, G., Katagiri, T., Sharma, K., Wilkinson, S., 2015. The 2015 Gorkha Nepal earthquake: insights from earthquake damage survey. Frontiers in Built Environment 1, 8. http://dx.doi.org/10.3389/fbuil.2015.00008.

Grandin, R., Vallée, M., Satriano, C., Lacassin, R., Klinger, Y., Simoes, M., Bollinger, L.B., 2015. Rupture process of the M_W 7.9 2015 Gorkha earthquake (Nepal): insights into Himalayan megathrust segmentation. Geophys. Res. Lett. 42, 8373–8382. http://dx.doi.org/10.1002/2015GL066044.

Hartzell, S.H., Heaton, T.H., 1983. Inversion of strong ground motion and teleseismic waveform data for the fault rupture history of the 1979 Imperial Valley, California, earthquake. Bull. Seismol. Soc. Am. 73 (6A), 1553–1583.

Hayes, G.P., Briggs, R.W., Barnhart, W.D., Yeck, W.L., McNamara, D.E., Wald, D.J., et al., 2015. Rapid characterization of the 2015 M_W 7.8 Gorkha, Nepal, earthquake sequence and its seismotectonic context. Seismol. Res. Lett. 86 (6), 1557–1567. http://dx.doi.org/10.1785/0220150145.

He, X., Ni, S., Ye, L., Lay, T., Liu, Q., Koper, K.D., 2015. Rapid seismological quantification of source parameters of the 25 April 2015 Nepal earthquake. Seismol. Res. Lett. 86 (6), 1568–1577. http://dx.doi.org/10.1785/0220150131.

Hough, S.E., 2015. Introduction to the focus section on the 2015 Gorkha, Nepal earthquake. Seismol. Res. Lett. 86 (6), 1502–1510.

Ishii, M., Shearer, P.M., Houston, H., Vidale, J.E., 2005. Extent, duration and speed of the 2004 Sumatra-Andaman earthquake imaged by the Hi-net array. Nature 435 (7044), 933–936.

Kanamori, H., Rivera, L., 2008. Source inversion of W phase: speeding up seismic tsunami warning. Geophys. J. Int. 175, 222–238. http://dx.doi.org/10.1111/j.1365-246X.2008.03887.x.

Kikuchi, M., Kanamori, H., 1991. Inversion of complex body waves—III. Bull. Seismol. Soc. Am. 81 (6), 2335–2350.

Kobayashi, T., Morishita, Y., Yarai, H., 2015. Detailed crustal deformation and fault rupture of the 2015 Gorkha earthquake, Nepal, revealed from ScanSAR-based interferograms of ALOS-2. Earth Planets Space 67, 201. http://dx.doi.org/10.1186/s40623-015-0359-z.

Krüger, F., Ohrnberger, M., 2005. Tracking the rupture of the $M_w = 9.3$ Sumatra earthquake over 1,150 km at teleseismic distance. Nature 435, 937–939. http://dx.doi.org/10.1038/nature03696.

Lindsey, E.O., Natsuaki, R., Xu, X., Shimada, M., Hashimoto, M., Melgar, D., Sandwell, D.T., 2015. Line-of-sight displacement from ALOS-2 interferometry: M_w 7.8 Gorkha earthquake and M_w 7.3 aftershock. Geophys. Res. Lett. 42, 6655–6661. http://dx.doi.org/10.1002/2015GL065385.

Liu, Z.-P., Ge, Z.-X., 2015. Rupturing process of the M_W 7.9 Nepal earthquake inverted by the multi-array compressive sensing method. Chin. J. Geophys. 58, 1891–1899. http://dx.doi.org/10.6038/cjg20150605.

Martin, S.S., Hough, S.E., Hung, C., 2015. Ground motions from the 2015 M_W 7.8 Gorkha, Nepal, earthquake constrained by a detailed assessment of macroseismic data. Seismol. Res. Lett. 86 (6), 1524–1532. http://dx.doi.org/10.1785/0220150138.

Meng, L., Zhang, A., Yagi, Y., 2016. Improving back-projection imaging with a novel physics-based aftershock calibration approach: a case study of the 2015 Gorkha earthquake. Geophys. Res. Lett. 43, 628–636. http://dx.doi.org/10.1002/2015GL067034.

Meng, L., Ampuero, J.-P., Luo, Y., Wu, W., Ni, S., 2012. Mitigating artifacts in back-projection source imaging with implications on frequency-dependent properties of the Tohoku-Oki earthquake. Earth Planets Space 64 (12), 1101–1109.

Moss, R.E.S., Thompson, E.M., Kieffer, D.S., Tiwari, B., Hashash, Y.M.A., Charya, I., et al., 2015. Geotechnical effects of the 2015 magnitude 7.8 Gorkha, Nepal, earthquake and aftershocks. Seismol. Res. Lett. 86 (6), 1514–1523. http://dx.doi.org/10.1785/0220150158.

Mugnier, J.-L., Gajurel, A., Huyghe, P., Jayangondaperumal, R., Jouanne, F., Upreti, B., 2013. Structural interpretation of the great earthquakes of the last millennium in the central Himalaya. Earth Sci. Rev. 127, 30–47.

Noda, H., Lapusta, N., Kanamori, H., 2013. Comparison of average stress drop measures for ruptures with heterogeneous stress change and implications for earthquake physics. Geophys. J. Int. 193, 1691–1712. http://dx.doi.org/10.1093/gji/ggt074.

Pérez-Campos, X., Singh, S.K., Beroza, G.C., 2003. Reconciling teleseismic and regional estimates of seismic energy. Bull. Seismol. Soc. Am. 93 (5), 2123–2130.

Sapkota, S.N., Bollinger, L., Klinger, Y., Tapponnier, P., Gaudemer, Y., Tiwari, D., 2013. Primary surface ruptures of the great Himalayan earthquakes in 1934 and 1255. Nat. Geosci. 6, 71–76.

Stevens, V.L., Avouac, J.-P., 2015. Interseismic coupling on the Main Himalayan Thrust. Geophys. Res. Lett. 42, 5828–5837. http://dx.doi.org/10.1002/2015GL064845.

Storchak, D.A., Di Giacomo, D., Bondár, I., Engdahl, E.R., Harris, J., Lee, W.H.K., Villaseñor, A., Bormann, P., 2013. Public release of the ISC-GEM global instrumental earthquake catalogue (1900–2009). Seismol. Res. Lett. 84 (5), 810–815. http://dx.doi.org/10.1785/0220130034.

VanDecar, J.C., Crosson, R.S., 1990. Determination of teleseismic relative phase arrival times using multi-channel cross-correlation and least squares. Bull. Seismol. Soc. Am. 80, 1548–1560.

Venkataraman, A., Kanamori, H., 2004. Observational constraints on the fracture energy of subduction zone earthquakes. J. Geophys. Res. 109, B05302. http://dx.doi.org/10.1029/2003JB002549.

Wang, D., Mori, J., 2016. Short-period energy of the 25 April 2015 M_W 7.8 Nepal earthquake determined from backprojection using four arrays in Europe, China, Japan, and Australia. Bull. Seismol. Soc. Am. 106 (1), 259–266. http://dx.doi.org/10.1785/0120150236.

Wang, K., Fialko, Y., 2015. Slip model of the 2015 M_W 7.8 Gorkha (Nepal) earthquake from inversions of ALOS-2 and GPS data. Geophys. Res. Lett. 42, 7452–7458. http://dx.doi.org/10.1002/2015GL065201.

Wang, W., Hao, J., He, J., Yao, Z., 2015. Rupture process of the M_W 7.9 Nepal earthquake April 25, 2015. Sci. China Earth Sci. 58, 1895–1900. http://dx.doi.org/10.1007/s11430-015-5170-y.

Xu, Y., Koper, K.D., Sufri, O., Zhu, L., R., H.A., 2009. Rupture imaging of the M_W 7.9 12 May 2008 Wenchuan earthquake from back projection of teleseismic P waves. Geochem. Geophys. Geosyst. 10, Q04006. http://dx.doi.org/10.1029/2008GC002335.

Yagi, Y., Okuwaki, R., 2015. Integrated seismic source model of the 2015 Gorkha, Nepal, earthquake. Geophys. Res. Lett. 42, 6229–6235. http://dx.doi.org/10.1002/2015GL064995.

Ye, L., Lay, T., Kanamori, H., Rivera, L., 2016. Rupture characteristics of major and great (M_W 7.0) megathrust earthquakes from 1990–2015: I. Source parameter scaling relationships. J. Geophys. Res. Solid Earth 121, 826–844. http://dx.doi.org/10.1002/2015JB012426.

Yin, J., Yao, H., Qin, W., Zeng-Lu, J., Zhang, H., 2016. Rupture processes and seismogenic mechanism of the 25 April 2015 Nepal M_W 7.8 earthquake. Earth Planet. Sci. Lett. (in revision).

Yun, S.-H., Hudnut, K., Owen, S., Webb, F., Simons, M., Sacco, P., et al., 2015. Rapid damage mapping for the 2015 M_W 7.8 Gorkha earthquake using synthetic aperture radar data from COSMO-SkyMed and ALOS-2 satellites. Seismol. Res. Lett. 86 (6), 1549–1556. http://dx.doi.org/10.1785/0220150152.

Zhang, G., Hetland, E., Shan, X., 2015. Slip in the 2015 M_W 7.9 Gorkha and M_W 7.3 Kodari, Nepal, earthquakes revealed by seismic and geodetic data: delayed slip in the Gorkha and slip deficit between the two earthquakes. Seismol. Res. Lett. 86 (6), 1578–1586. http://dx.doi.org/10.1785/0220150139.